An unbiased study of debris discs around A-type stars with *Herschel*

N. D. Thureau,[1]★ J. S. Greaves,[1] B. C. Matthews,[2,3] G. Kennedy,[4] N. Phillips,[5] M. Booth,[2,3,6] G. Duchêne,[7,8] J. Horner,[9,10,11] D. R. Rodriguez,[12] B. Sibthorpe[13] and M. C. Wyatt[4]

[1]*School of Physics and Astronomy, University of St Andrews, North Haugh, St Andrews KY16 9SS, UK*
[2]*National Research Council Herzberg Astronomy and Astrophysics, 5071 West Saanich Road, Victoria, BC V9E 2E7, Canada*
[3]*Department of Physics & Astronomy, University of Victoria, Elliott Building, 3800 Finnerty Road, Victoria, BC V8P 5C2, Canada*
[4]*Institute of Astronomy, Madingley Road, Cambridge CB3 0HA, UK*
[5]*Joint ALMA Observatory, Alonso de Córdova 3107 Vitacura, Santiago, Chile*
[6]*Instituto de Astrofísica, Pontificia Universidad Católica de Chile, Vicuña Mackenna 4860, 7820436 Macul, Santiago, Chile*
[7]*Astronomy Department, UC Berkeley, Hearst Field Annex B-20, Berkeley, CA 94720-3411, USA*
[8]*Univ. Grenoble Alpes/CNRS, IPAG, F-38000 Grenoble, France*
[9]*School of Physics, University of New South Wales, Sydney 2052, Australia*
[10]*Australian Centre for Astrobiology, University of New South Wales, Sydney 2052, Australia*
[11]*Computational Engineering and Science Research Centre, University of Southern Queensland, Toowoomba, Queensland 4350, Australia*
[12]*Departamento de Astronomia, Universidad de Chile, Casilla 36-D, Santiago, Chile*
[13]*SRON Netherlands Institute for Space Research, Landleven 12, NL-9747 AD Groningen, the Netherlands*

ABSTRACT

The *Herschel* DEBRIS (Disc Emission via a Bias-free Reconnaissance in the Infrared/Submillimetre) survey brings us a unique perspective on the study of debris discs around main-sequence A-type stars. Bias-free by design, the survey offers a remarkable data set with which to investigate the cold disc properties. The statistical analysis of the 100 and 160 μm data for 86 main-sequence A stars yields a *lower* than previously found debris disc rate. Considering better than 3σ excess sources, we find a detection rate $\geq 24 \pm 5$ per cent at 100 μm which is similar to the debris disc rate around main-sequence F/G/K-spectral type stars. While the 100 and 160 μm excesses slowly decline with time, debris discs with large excesses are found around some of the oldest A stars in our sample, evidence that the debris phenomenon can survive throughout the length of the main sequence (∼1 Gyr). Debris discs are predominantly detected around the youngest and hottest stars in our sample. Stellar properties such as metallicity are found to have no effect on the debris disc incidence. Debris discs are found around A stars in single systems and multiple systems at similar rates. While tight and wide binaries (<1 and >100 au, respectively) host debris discs with a similar frequency and global properties, no intermediate separation debris systems were detected in our sample.

Key words: surveys – binaries: general – circumstellar matter – stars: individual: A-stars – infrared: stars.

1 INTRODUCTION

Debris discs, analogues to the Solar system asteroid (O'Brien & Sykes 2011) and Edgeworth–Kuiper (Lykawka 2012) belts, are comprised of objects the size of dwarf planets down to submicron dust particles. Their evolution can be affected strongly by the presence of planets (Hahn & Malhotra 2005; Morbidelli et al. 2005; Lykawka et al. 2009), therefore one can gain a better understanding of planet formation processes through the study of debris discs with

a systematic unbiased examination of the frequency of debris discs and statistical analysis of their properties.

Debris discs are produced from the destruction of bodies created during the planet formation process. They are less massive than protoplanetary discs ($\lesssim 1\,M_{\oplus}$ of dust; Panić et al. 2013) and contain very little or no gas. Dust emission from debris discs is readily observable due to their large surface area. The dust originates from collisional cascades possibly initiated by the stirring of the smaller population of planetesimals by larger objects (Kenyon & Bromley 2002). The dust grains are heated by the central star and produce thermal emission that can be best detected in the form of a mid- and far-infrared excess where the contrast between the thermal emission of the star and the dust is most favourable.

★ E-mail: nt15@st-andrews.ac.uk

The first debris discs were discovered (Aumann et al. 1984; Aumann 1985) with the space-based telescope *IRAS* (*Infrared Astronomical Satellite*) through the detection of large far-infrared excesses around the stars Vega, Fomalhaut, ϵ Eridani and β Pictoris. Following these pioneering results, a number of surveys dedicated to the detection and analysis of debris discs were performed with space-based instruments [e.g. *ISO* (*Infrared Space Observatory*), *Spitzer*] or ground-based telescopes in the near- and mid-infrared and submillimetre.

This paper presents results from the DEBRIS (Disc Emission via a Bias-free Reconnaissance in the Infrared/Submillimetre) survey which was carried out with the space telescope *Herschel* (Pilbratt et al. 2010) as part of the open time key programmes. The *Herschel* telescope is particularly well suited for the observation of debris discs due to its 70–500 µm wavelength range, sensitivity and angular resolution. The DEBRIS survey observed a volume-limited sample (within ∼45 pc of the sun) of 446 debris candidates with spectral types ranging from A to M. We direct the interested reader to Phillips et al. (2010); Matthews & Kavelaars (2010) and Matthews et al. (in preparation) for a detailed description of the survey. The *Herschel* images of discs around stars of varying ages provide a measure of how dust evolves and a measure of internal disc structure assuming a similar grain destruction mechanism is taking place in all discs in our sample.

The incidence of debris discs is typically expected to depend on the spectral type of their host stars as a result of the discs detectability being a function of the spectral type (Wyatt 2008) and the differences in physical properties of the discs such as the mass distribution (Greaves & Wyatt 2003) or the dust evolution (Plavchan, Jura & Lipscy 2005). For that reason, the results for sun-like stars (spectral types F, G and K) and M stars are treated separately in Sibthorpe et al. (in preparation) and Lestrade et al. (in preparation). In this paper, we present the 100 and 160 µm photometric flux-limited observations of the subsample of 83 A-type primary stars made with PACS (Photodetector Array Camera and Spectrometer). A detailed presentation of PACS in given by Poglitsch et al. (2010).

A-type stars, due to their high stellar luminosities, are ideal candidates to study the evolution of debris discs in the far-infrared with previous studies reporting debris disc rates as high as 67 per cent (with a 33 per cent lower limit; Su et al. 2006) and 41 per cent (Phillips 2011).

2 EXCESS DETECTION

Our sample consists of 83 stars with spectral type A. The sample is unbiased with respect to stellar properties and complete to 45 pc excepting stars with high cirrus confusion level (Phillips et al. 2010). A summary of the observations is given in Table 1. For each candidate, photometry measurements were derived from the PACS 100 and 160 µm maps. The spectral energy distribution (SED hereafter) of each system was computed based on the PACS photometry data and data from the literature (see Table B1 for a complete list of references). At wavelengths shorter than 9 µm, the stellar photosphere is modelled using the PHOENIX *Gaia* grid with the best-fitting model being found by least-squares minimization. At wavelengths longer than 9 µm, the excess emission is modelled with a modified blackbody function where, for wavelengths greater than λ_0, the blackbody is multiplied by $(\lambda/\lambda_0)^{-\beta}$. The disc is modelled with one or two blackbody components depending on the goodness of the fit. See Kennedy et al. (2012) for more details. The SED fits for the DEBRIS targets are shown in Fig. 1. The photospheric fluxes, P_{100} and P_{160}, derived from the SED modelling, were then compared to the measured fluxes, F_{100} and F_{160}, in order to detect the infrared excess signature of potential debris discs.

The cumulative distribution functions of the observed to photospheric flux ratios $R_\lambda = \frac{F_\lambda}{P_\lambda}$ are shown in Figs 2(a) and (b) as solid lines. The red double-dot–dashed lines show the fraction of stars for which, at a given R_λ level, the photospheric flux would have been confidently detected. The fraction of stars where these lines cross $R_\lambda = 1$ indicates the fraction of photospheres that would have been detected with 3σ significance at each wavelength. We find this fraction to be 66 per cent at 100 µm, and 12 per cent at 160 µm. The green dash–dotted lines give the fraction of stars for which an excess at a $3 \times e_\lambda$ level could have been confidently detected, had it been present. Where $e_\lambda = (e_{F_\lambda}^2 + e_{P_\lambda}^2)^{1/2}$ with e_{F_λ} and e_{P_λ} being the individual errors on the flux and photospheric values, respectively, and e_{F_λ} the dominant source of error. For example, at 100 µm $e_{F_{100}}$ is typically $5 \times$ larger than $e_{P_{100}}$ for $F_{100} > 2$ mJy. Thus, the medians of these lines indicate the typical disc detection limit we achieve in the observations. As such, we find that the median disc detection limits of our survey are $R_{100}^{det} = 1.70$ and $R_{160}^{det} = 3.87$ at 100 and 160 µm, respectively. The median detection limits are indicated as dashed vertical lines in our graphs. The long-dash lines are lognormal fits to the $R_\lambda < 1$ values which, given that these must be noise and under the assumption that positive noise is as likely as negative noise, indicates the fraction of positive detections we might expect due to the noise. That fraction rapidly decreases to zero, and is below 0.5 per cent for $R_{100} > R_{100}^{det}$ and below 1 per cent for $R_{160} > R_{160}^{det}$.

For each debris candidate, the flux excess significance χ_λ was calculated and used to determine whether a source has a disc detection. The excess significance at a wavelength λ, χ_λ, is defined as

$$\chi_\lambda = \frac{F_\lambda - P_\lambda}{(e_{F_\lambda}^2 + e_{P_\lambda}^2)^{1/2}}$$

A disc is detected in a system when $\chi_\lambda \geq 3$. The distributions of χ_{100} and χ_{160} are shown in Figs 3(a) and (b).

Amongst our targets, we have 18 disc detections at 100 µm and 12 disc detections at 160 µm. No disc was detected solely at 160 µm. One of the DEBRIS targets, 38 Ari (A077A, HD 17093), was found to have an excess at 160 µm only. However, based on DEBRIS and SCUBA-2 (Submillimetre Common-User Bolometer Array) data, Panić et al. (2013) conclude that the emission originates from a background galaxy. The measured fluxes and modelled photometry as well as the excesses and excess significance for the 18 debris systems are listed in Table 2 with the nine resolved discs (see Booth et al. 2013) being marked with asterisk. These discs will hereafter be referred to as group I discs. Moreover, three more discs are included in our analysis throughout the paper: the debris discs around Vega (Sibthorpe et al. 2010), Fomalhaut (Acke et al. 2012) and β Pic (Vandenbussche et al. 2010). These stars are within our unbiased volume and were only excluded from DEBRIS because they were *Herschel* guaranteed time targets. Consequently, we find that the disc detection rates are: $21/86 = 24 \pm 5$ per cent at 100 µm and $15/86 = 17 \pm 4$ per cent at 160 µm. The debris disc detection rates errors are binomial uncertainties and are used throughout the paper. The debris discs frequency is consistent with that found by the DUst around NEarby Stars (DUNES) survey for solar type stars where for F/G/K stars, significant infrared excess was detected around 25 of the 124 stars from their sample (20.2 per cent), see Eiroa et al. (2013).

The aforementioned DEBRIS disc incidence assumes that none of the stars with $\chi_\lambda < 3$ have a disc, which underestimates the actual disc incidence amongst the A-star population. Although it

Table 1. Observations summary. Bold DEBRIS names indicate multiple sources. A complete study of the multiplicity of the DEBRIS stars was performed by Rodriguez et al. (in preparation).

| DEBRIS name	ID	Observing date	Obs. ID scan/cross-scan	DEBRIS name	ID	Observing date	Obs. ID scan/cross-scan
A002	HD 187642	05-09-2010	1342196032/33	A066	HD 104513	12-23-2010	1342211432/33
A005	HD 102647	11-30-2009	1342187365/–	A067	HD 14055	07-10-2011	1342223876/77
A006	HD 60179	05-09-2010	1342196014/15	A068	HD 91312	05-16-2011	1342221156/57
A007	HD 76644	05-22-2010	1342196857/58	**A069**	HD 112413	12-07-2009	1342187807/–
A011	HD 97603	12-23-2010	1342211428/29	A071	HD 109536	08-09-2010	1342202333/34
A012	HD 11636	02-12-2011	1342214157/58	**A073**	HD 16754	02-12-2011	1342214183/84
A013	HD 115892	08-16-2010	1342203106/07	A074	HD 79439	11-10-2010	1342209358/59
A015	HD 141795	09-09-2010	1342204160/61	A076	HD 110411	01-15-2011	1342212660/61
A016	HD 38678	09-27-2010	1342205200/01	A077	HD 17093	07-10-2011	1342223856/57
A017	HD 118098	02-01-2011	1342213610/11	A078	HD 184006	05-05-2010	1342195831/32
A018	HD 139006	02-07-2011	1342213794/95	A079	HD 102124	05-29-2011	1342221861/62
A019	HD 156164	03-30-2010	1342193061/62	A080	HD 177196	05-05-2010	1342195829/30
A020	HD 130841	02-08-2011	1342213840/41	A082	HD 71155	05-10-2010	1342196127/28
A021	HD 2262	04-29-2011	1342220764/65	**A083**	HD 80081	11-11-2010	1342209370/71
A022	HD 197157	05-09-2010	1342196039/40	A084	HD 78045	03-30-2010	1342193046/47
A023	HD 16970	02-26-2011	1342215729/30	**A086**	HD 13161	07-04-2011	1342223650/51
A024	HD 95418	05-24-2010	1342197015/16	A087	HD 95608	12-16-2010	1342212017/18
A026	HD 106591	06-22-2010	1342199127/28	A089	HD 215789	05-21-2010	1342196801/02
A028	HD 116656	01-08-2011	1342212395/96	A090	HD 5448	02-12-2011	1342214163/64
A029	HD 99211	01-10-2011	1342212475/76	A091	HD 137898	09-09-2010	1342204154/55
A032	HD 103287	06-22-2010	1342199121/22	A092	HD 165040	10-25-2010	1342207069/70
A034	HD 165777	03-22-2011	1342216601/02	**A093**	HD 110304	07-03-2011	1342223606/07
A035	HD 108767	01-17-2011	1342212822/23	A095	HD 109787	08-12-2010	1342202925/26
A036	HD 176687	04-22-2010	1342195364/65	A096	HD 154494	10-07-2010	1342206007/08
A038	HD 18978	06-23-2011	1342223496/97	A098	HD 85376	11-05-2010	1342209079/80
A039	HD 180777	05-09-2010	1342196021/22	A101	HD 130109	02-07-2011	1342213814/15
A040	HD 33111	03-31-2010	1342193123/24	**A103**	HD 1404	02-08-2011	1342213948/49
A041	HD 210418	05-05-2010	1342195835/36	A104	HD 90132	12-16-2010	1342211989/90
A042	HD 87696	12-01-2010	1342210616/17	A105	HD 19107	07-03-2011	1342223584/85
A043	HD 172555	04-18-2011	1342218804/05	A106	HD 210049	05-21-2010	1342196795/96
A045	HD 78209	05-22-2010	1342196859/60	**A107**	HD 165189	03-30-2010	1342193042/43
A048	HD 125161	01-10-2011	1342212442/43	**A109**	HD 223352	05-16-2011	1342221122/23
A049	HD 50241	08-27-2010	1342203663/64	A110	HD 89021	12-01-2010	1342210614/15
A051	HD 202730	03-25-2010	1342192757/58	A113	HD 23281	08-09-2010	1342202300/01
A052	HD 159560	05-21-2010	1342196785/86	A118	HD 15008	09-10-2010	1342204270/71
A053	HD 125162	12-09-2010	1342210928/29	A119	HD 212728	05-10-2010	1342196109/10
A056	HD 56537	10-25-2010	1342207153/54	A120	HD 186219	11-12-2010	1342208855/56
A057	HD 88955	12-16-2010	1342211987/88	A121	HD 222345	05-16-2011	1342221114/15
A061	HD 188228	09-10-2010	1342204276/77	**A123**	HD 213398	05-21-2010	1342196807/08
A063	HD 222603	05-28-2011	1342221790/91	**A127**	HD 140436	02-07-2011	1342213792/93
A064	HD 20320	03-05-2011	1342216125/26	**A130**	HD 16555	03-31-2010	1342193105/06
A065	HD 137909	02-07-2011	1342213790/91				

is not possible to infer the actual disc rate from our data sample, but only a lower limit, we can derive an upper limit by assuming that all the stars with $\chi_\lambda < 3$ have an excess equal to $3 \times e_\lambda$. The CDFs of $X_\lambda = R_\lambda - 1$ are shown in Figs 4(a) and (b). The double-dot–dashed line illustrates the lower limit where we assume that none of the stars with $\chi_\lambda < 3$ have a disc while the topmost dotted line represents the upper limit where we assume that all the stars with $\chi_\lambda < 3$ have an excess equal to $3 \times e_\lambda$. The true distribution should lie within the greyed area of the plot. At the median detection threshold $X_{100} = 0.70$, of the full A-stars sample, 21 discs were detected while there are 23 stars above this level with no detection ($\chi_{100} < 3$). The lower limit gives a disc detection rate of 21/86 (24 per cent) while the upper limit gives a disc detection rate of 44/86 (51 per cent).

A few systems where Multiband Imaging Photometer for Spitzer (MIPS)-70 observations showed evidence of a debris disc excess (Phillips 2011) did not meet the χ_{100} detection

criterion: ι Cen (A013A), ι Ind (A051A), 25 Dra (A052A), q Vel (A057A), s Eri (A073A), 60 Leo (A087A), 14 PsA (A106A) and HR 7498 (A120A). Small excesses, below the χ_{100} detection threshold, are measured for some of these systems: specifically, ι Cen ($\chi_{100} = 2.08$), ι Ind ($\chi_{100} = 2.62$), q Vel ($\chi_{100} = 2.06$), 60 Leo ($\chi_{100} = 1.74$) and HR 7498 ($\chi_{100} = 1.07$). These systems will hereafter be referred as group II objects. We believe these stars do have discs but with a 100 µm flux that lies below our threshold. In the case of 25 Dra, s Eri and 14 PsA, no excess was detected; however, we can now identify two point sources where only one was found with the ∼20 arcsec full width at half-maximum (FWHM) MIPS-70 beam. The 100 µm maps for these three objects are shown in Fig. 5. These systems will hereafter be referred to as group III objects. Aperture photometry carried out with GAIA (Graphical Astronomy and Image Analysis Tool) on the DEBRIS 100 µm maps, using an 8 arcsec-radius aperture (matching the first null of a 6.7 arc-sec FWHM beam) and a 0.66 aperture correction factor, shows
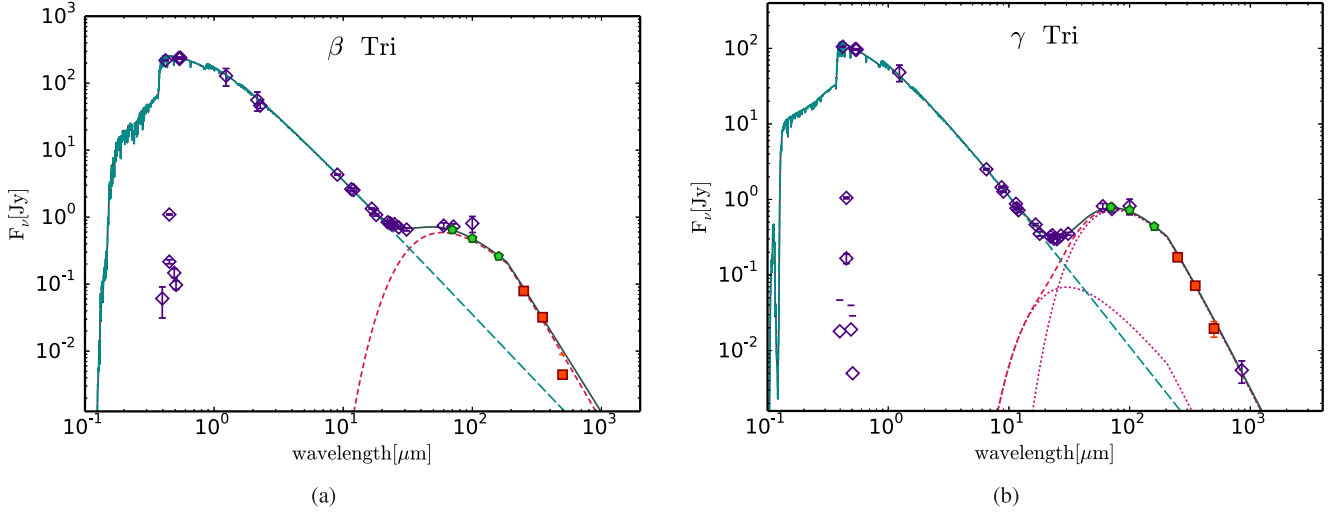
Figure 1. SEDs for the DEBRIS targets with confirmed debris discs. (a) SED for β Tri. (b) SED for γ Tri. Photometry is shown as open diamond (data from the literature), green pentagons (PACS photometry) and red squares (SPIRE photometry). The stellar spectrum is shown as a blue long-dash line and the blackbody disc model as a red short-dash line, with the total shown as a solid line. Where the best blackbody disc model consists of two components, individual disc models are shown as red dotted lines. The full set of SED plots (DEBRIS group I targets listed in table 3) will be available in the online edition of the journal.
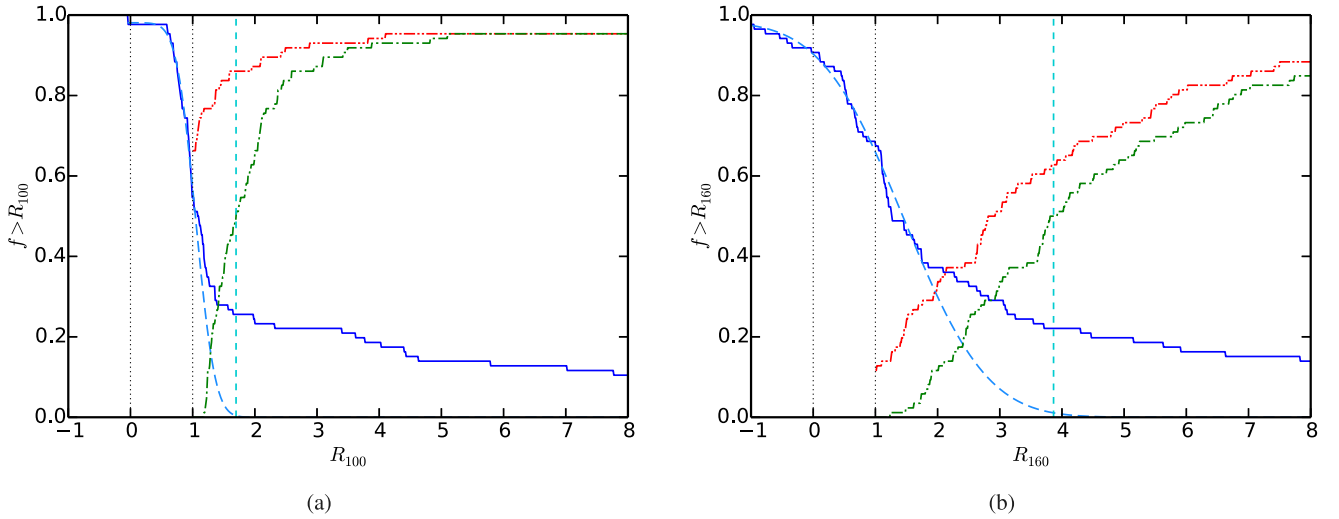
Figure 2. (a) Solid line: the cumulative distribution function (CDF) of R_{100}. Double-dot–dashed line: fraction of stars with $P_{100} > \frac{3 \times e_{100}}{R_{100}}$ as a function of R_{100}. Dash–dotted line: fraction of stars for which disc emission could have been detected at this level (i.e. $F_{100}^{\text{disc}} > \frac{3 \times e_{100}}{R_{100}}$) as a function of R_{100}. F_{100}^{disc} is the measured 100 μm disc flux. Long-dash curve: lognormal fit to the $R_{100} < 1$ values. The R_{100} CDF departs from the fit for $R_{100} = 1.05$, while the R_{160} CDF departs from the fit for $R_{160} = 1.81$. The vertical short-dash line indicates the 3σ $R_{100}^{\text{det}} = 1.70$ median detection limit. The vertical dotted lines indicate the $R_{100} = 0$ and $=1$ values. (b) Same as (a) for wavelength 160 μm where the 3-σ median detection limit is $R_{160}^{\text{det}} = 3.87$.

that there is at least one background source within the MIPS-70 beam with enough flux to explain the excesses that were detected with MIPS-70. The aperture photometry measurements, made on PACS-100 maps, for the three aforementioned DEBRIS targets are summarized in Table 3.

3 PROPERTIES OF A-STAR DEBRIS DISCS

3.1 Disc temperature and fractional luminosity

Two fundamental observable parameters of a debris disc are its temperature T_{disc} and its fractional luminosity f_{d}. The fractional luminosity is defined as the ratio of the luminosity from the dust to that of the star, $f_{\text{d}} = L_{\text{disc}}/L_*$. The disc temperatures derived from the SED model fitting are listed in Table 4. In most cases, the best-fitting model consisted of a single temperature cold disc model, with the exception of Vega (A003A), Fomalhaut (A004A), β Pic (A014A), λ Boo (A053A), γ Tri (A067A), ρ Vir (A076A), 30 Mon (A082) and δ Scl (A109AB) where the best-fitting model consisted of two components (cold and hot) disc model. The cold disc temperatures found range from 37 to 289 K with a median value of 110 K, which is within the expected 10 K up to a few hundred K range for debris discs (Wyatt 2008). For comparison, the surface temperatures in the Edgeworth–Kuiper belt are lower ~50 K (Jewitt & Luu 2004) although crystallinity present in the belt indicates that
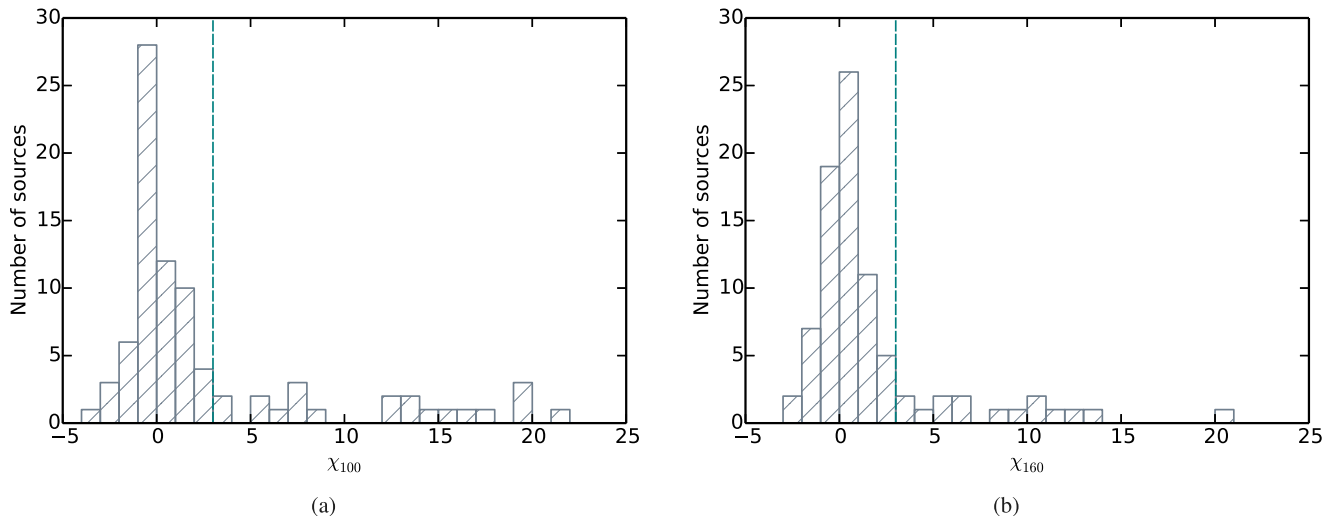
Figure 3. (a) Distribution of the 100 μm fluxes formal significance χ_{100}. The dashed vertical line indicates the $\chi_{100} = 3$ detection threshold. (b) Same as (a) for wavelength 160 μm.

it has been heated to $\gtrsim 110$ K. The temperature distribution for the cold disc components from groups I and II is shown in Fig. 6.

The fractional luminosity is a quantity used to estimate the amount of dust present in the debris disc systems. It measures the fraction of the stellar radiation that will be absorbed by the dust and re-emitted in the infrared. A histogram of the total fractional luminosity is shown in Fig. 7. Where the best blackbody disc model consists of two components, the total fractional luminosity is the sum of of the fractional luminosities of both disc components: $f_d = f_d^{cold} + f_d^{hot}$. The values range from $\sim 4.4 \times 10^{-6}$ to $\sim 3.2 \times 10^{-3}$ with a median (mean) for our sample being $\approx 2.7 \times 10^{-5}$ ($\approx 2.2 \times 10^{-4}$). The distribution can be compared to that found by Su et al. (2006, fig. 10), where the median fractional luminosity found was $\approx 5.0 \times 10^{-5}$ for their A-star sample observed with *Spitzer*. The faintest detected disc has a fractional luminosity $f_d = 0.44 \times 10^{-5}$ which can be compared to the fractional luminosity of the Edgeworth–Kuiper belt, which was estimated by Vitense et al. (2012) to be about 10^{-7} (100× fainter).

Moreover, under the assumption of a steady-state collisional evolution model, for a given stellar age, there is a maximum disc mass, and also fractional luminosity f_{max}, that can remain due to collisional processing. We use the definition of f_{max} given by Wyatt (2008) equation 18:

$$f_{max} = 0.58 \times 10^{-9} R_{disc}^{7/3} \left(\frac{dR_{disc}}{R_{disc}} \right) D_c^{1/2} Q_D^{*5/6} e^{-5/3} M_*^{-5/6} L_*^{-1/2} t_{age}^{-1},$$

where dR_{disc} is the width of the disc in au, D_c is the size of the planetesimal feeding the cascade in km, Q_D^* is the planetesimal strength in J kg^{-1}, e is the mean planetesimal eccentricity, M_* is the stellar mass in M$_\odot$, L_* is the stellar luminosity in L$_\odot$ and t_{age} is the age of the system in Myr. The calculations are conducted assuming $dR_{disc}/R_{disc} = 0.5$, $D_c = 60$ km, $Q_D^* = 150$ J kg^{-1} and $e = 0.05$.

Hence stars older than the collisional time should have a fractional luminosity equal to f_{max}. The ratios of f_d/f_{max} are given in Table 4. The large spread of the values is expected to arise from the different planetesimal properties of the systems. However, an anomalously high dust content, $f_d \gg f_{max}$, can be associated with systems undergoing transient events. In our sample, five discs have a high f_d/f_{max} ratio: β Pic (A014A), ζ Lep (A016A), 21 LMi (A042A), HR 7012 (A043A), HR 1139 (A113A). Since these five stars have a black-

body disc radius ≤ 20 au, a high ratio would be normal were the stars younger than ~ 10 Myr as is the case for β Pic and HR 7012. However, for the remaining stars, the ratios are not high enough to conclude on the transient nature of the dust.

3.2 Disc radius

If one assumes a disc made of blackbody like dust grains with a temperature T_{disc} uniformly distributed in a thin torus of radius R_{disc} and negligible width around a star of radius R_* and effective temperature T_*, R_{disc} can be derived from the following relationship (Backman & Paresce 1993): $R_{disc} = 0.5R_*(T_*/T_{disc})^2$. We list the values of the disc radii in Table 4. The distribution of radii inferred from our observations is shown in Fig. 8. The derived radii, R_{disc}^{cold}, range from 3 to 236 au with a median (mean) disc radius value of $\tilde{R}_{disc}^{cold} \sim 38$ au ($\bar{R}_{disc}^{cold} \sim 64$ au). However, disc temperatures can be hotter than blackbody temperature because the emission is dominated by the smallest grains, whose temperatures can be hotter than blackbody due to long-wavelength emission inefficiency. As such a blackbody disc radius is only a representative measure, and we expect discs to be a factor of a few larger than this. Booth et al. (2013) in their fig. 6 show the resolved radii plotted against blackbody radii for a few DEBRIS A stars. See also Rodriguez & Zuckerman (2012) for a detailed analysis of the resolved to blackbody radii ratios. They found a median resolved to blackbody disc radii ratio of ~ 3.4. Resolved and blackbody radii are listed in table 7 and shown in fig. 9 of Rodriguez & Zuckerman (2012).

The lack of discs with small radii (i.e. <10 au) arises both from the excess detection limits and the age of our unbiased debris discs with 16/21 stars in the 100–800 Myr range. These limitations on the range of observable disc radii were demonstrated by Wyatt et al. (2007) and are illustrated here in Fig. 9 which can be compared to fig. 4 from Wyatt et al. (2007). Fig. 9 shows fractional luminosity as a function of the blackbody disc radius. The dashed (dotted) lines show the expected maximum fractional luminosity, $f_{max} \propto R_{disc}^{7/3}$, as defined by equation 18 from Wyatt (2008), for the 10, 100 and 1000 Myr old debris discs around A0 (A9) stars that are sustained by the collisional processing. Both lines are for the median excess detection threshold. For example, discs older than 100 Myr should lie below the 100 Myr maximum luminosity line. The solid line

Table 2. Observed and predicted PACS photometry. Group I: DEBRIS targets with confirmed disc detections. Asterisks (*) indicate the discs that are resolved with PACS (see Booth et al. 2013 for more details). Group II: DEBRIS targets that had a confirmed disc detection with MIPS-70 but do not meet the detection threshold with PACS-100/160. Group III: DEBRIS targets that had a confirmed disc detection with MIPS-70 which is now rejected due to a nearby background source at the time unresolved. The *Herschel* guaranteed time targets – Vega, Fomalhaut and β Pic – are included in the last section of the table. Values for the DEBRIS targets with no disc detection are listed in the appendix. References for stellar ages: (1) Zuckerman et al. (2011), (2) Nielsen et al. (2013), (3) King et al. (2003), (4) Zuckerman et al. (2006), (5) Vican (2012), (6) Rebull et al. (2008), (7) Monnier et al. (2012), (8) Mamajek (2012). Known groups/associations are quoted in column 7. Since no measurements were taken at 100 μm for Fomalhaut, the $F100$ value quoted in the table is colour corrected IRAS 100 μm flux.

DEBRIS name	Name	ID	Spectral type	Distance (parsec)	Age (Myr)	Group (Ref)	$F100$ (mJy)	$P100$ (mJy)	$R100$	χ_{100}	$F160$ (Jy)	$P160$ (Jy)	$R160$	χ_{160}
						Group I								
A005A	β Leo	HD 102647	A3Va	11.01	40	Argus (1)	475.54 ± 29.72	67.73 ± 1.34	7.02	13.71	204.15 ± 30.38	26.08 ± 0.52	7.83	5.86
A016A	ζ Lep	HD 38678	A2IV–V(n)	21.61	280	(2, 5)	115.88 ± 6.98	20.03 ± 0.63	5.79	13.69	33.22 ± 4.52	7.74 ± 0.24	4.29	5.63
A018A(*)	α CrB	HD 139006	A0V	23.01	450	UMa (3, 4)	225.33 ± 11.51	51.18 ± 0.85	4.40	15.09	61.47 ± 3.19	19.69 ± 0.33	3.12	13.04
A021A	κ Phe	HD 2262	A5IVn	23.81	609	(2, 5)	30.49 ± 2.87	15.45 ± 0.32	1.97	5.22	7.05 ± 3.97	5.96 ± 0.12	1.18	0.27
A024A(*)	β UMa	HD 95418	A1V	24.45	450	UMa (3, 4)	183.05 ± 43.58	45.42 ± 0.77	4.03	3.16	53.92 ± 15.72	17.48 ± 0.30	3.09	2.32
A042A	21 LMi	HD 87696	A7V	28.24	450	UMa (3, 4)	22.07 ± 2.36	9.52 ± 0.61	2.32	5.15	9.65 ± 3.40	3.67 ± 0.23	2.63	1.75
A043A	HR 7012	HD 172555	A7V	28.54	12	β pic (6)	94.72 ± 5.87	7.33 ± 0.66	12.91	14.80	45.48 ± 5.11	2.83 ± 0.25	16.08	8.34
A053A(*)	λ Boo	HD 125162	A3Va	30.36	290	(5)	273.44 ± 15.08	11.03 ± 0.20	24.78	17.40	137.01 ± 11.58	4.26 ± 0.08	32.17	11.47
A061A(*)	ϵ Pav	HD 188228	A0Va	32.22	40	Argus (1)	41.70 ± 4.58	9.42 ± 0.18	4.43	7.05	24.00 ± 3.25	3.62 ± 0.07	6.63	6.26
A064A(*)	ζ Eri	HD 20320	A9m–A9V	33.65	800	(5)	84.13 ± 5.90	8.48 ± 0.20	9.92	12.81	42.93 ± 3.06	3.27 ± 0.08	13.12	12.96
A067A(*)	γ Tri	HD 14055	A1Vnm	34.4	160	(5)	723.85 ± 35.74	11.31 ± 0.32	64.01	19.94	437.89 ± 10.26	4.37 ± 0.12	100.16	42.26
A076A(*)	ρ Vir	HD 110411	A3Va	36.26	295	(2, 5)	153.25 ± 6.96	5.46 ± 0.10	28.06	21.24	64.17 ± 6.67	2.11 ± 0.04	30.43	9.30
A082A(*)	30 Mon	HD 71155	A0V	37.51	223	(2, 5)	83.11 ± 5.67	10.71 ± 0.23	7.76	12.76	23.15 ± 2.72	4.12 ± 0.09	5.62	6.98
A086A(*)	β Tri	HD 13161	A5III	38.87	730	(5)	480.23 ± 22.96	35.31 ± 0.67	13.60	19.37	260.12 ± 11.82	13.62 ± 0.26	19.10	20.84
A103A	σ And	HD 1404	A2V	41.29	450	(5)	25.48 ± 2.65	7.49 ± 0.18	3.40	6.76	12.94 ± 4.10	2.89 ± 0.07	4.47	2.45
A109AB	δ Scl	HIP 117452	A0V	42.11	70	AB Dor (1)	28.89 ± 2.85	6.25 ± 0.18	4.62	7.94	−0.08 ± 3.26	2.41 ± 0.07	−0.03	−0.76
A113A	HR 1139	HD 23281	A5m	42.39	390	(5)	13.66 ± 2.54	3.63 ± 0.08	3.76	3.95	12.57 ± 5.49	1.40 ± 0.03	8.97	2.04
A123A	β PsA	HD 213398	A0V	43.8	180	(5)	28.47 ± 2.61	7.87 ± 0.20	3.62	7.88	3.32 ± 3.56	3.04 ± 0.08	1.09	0.08
						Group II								
A013A	ι Cen	HD 115892	A3m–A3va	18.02	306	(2, 5)	38.98 ± 2.94	32.75 ± 0.57	1.19	2.08	15.85 ± 6.23	12.58 ± 0.22	1.26	0.52
A051A	ι Ind	HD 198308	A5V(n)	30.2561	600	(5)	17.29 ± 3.22	8.66 ± 0.69	2.00	2.62	10.67 ± 5.32	3.34 ± 0.27	3.20	1.38
A057A	q Vel	HD 88955	A2Va	31.08	40	Argus (1)	16.89 ± 2.12	12.48 ± 0.27	1.35	2.06	8.89 ± 4.19	4.80 ± 0.11	1.85	0.98
A087A	60 Leo	HD 95608	A1m	38.96	320	(5)	10.80 ± 1.82	7.61 ± 0.20	1.42	1.74	3.60 ± 2.98	2.93 ± 0.08	1.23	0.22
A120A	HR 7498	HD 186219	A4III	43.58	580	(5)	7.39 ± 2.49	4.72 ± 0.08	1.57	1.07	10.73 ± 6.78	1.82 ± 0.03	5.89	1.31
						Group III								
A052A	25 Dra	HD 159560	A4m	30.35	700	(5)	7.88 ± 2.75	8.36 ± 0.13	0.94	−0.17	5.14 ± 4.11	3.22 ± 0.05	1.59	0.47
A073A	s Eri	HD 16754	A1Vb	35.72	30	Tuc/Hor (1)	5.32 ± 1.87	6.59 ± 0.11	0.81	−0.68	6.37 ± 4.48	2.55 ± 0.04	2.50	0.85
A106A	μ PsA	HD 210049	A1.5IVn	41.59	390	(5)	5.97 ± 1.66	7.19 ± 0.14	0.83	−0.73	4.82 ± 3.84	2.77 ± 0.05	1.74	0.53
						Herschel guaranteed time targets								
A003A	Vega	HD 172167	A0Va	7.68	700	(7)	5844 ± 336	405.43 ± 7.51	14.41	16.16	4430 ± 865	156.27 ± 2.89	28.35	4.94
A004A	Fomalhaut	HD 216956	A4V	7.7	478	(2, 8)	10970 ± 1300	161.56 ± 3.10	67.90	8.31	6067 ± 587	62.16 ± 1.19	97.61	10.23
A014A	β Pic	HD 39060	A6V	19.44	12	(6)	9753 ± 498	16.43 ± 0.89	593.59	19.57	4948 ± 485	6.34 ± 0.34	780.30	10.19
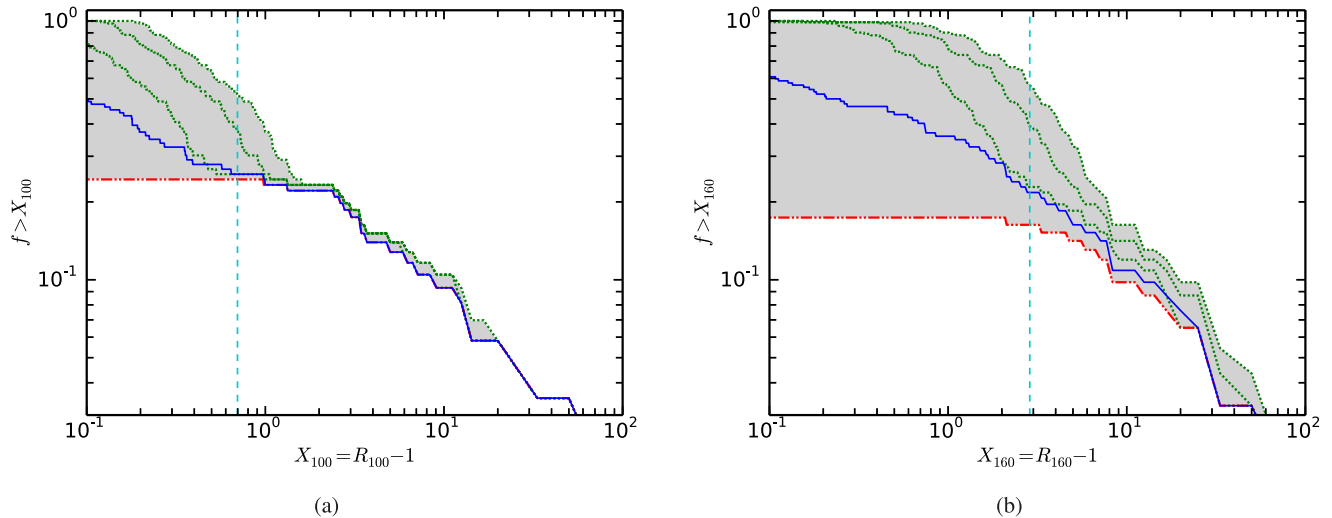
Figure 4. (a) The CDF of $X_{100} = R_{100} - 1$ for the entire DEBRIS sample including the three GTO targets is shown as a solid line. The same distribution for the disc population is expected to lie within the greyed area of the graph. The upper limit, topmost dotted line, is derived assuming that all the stars with $\chi_{100} < 3$ have excesses at the level of $3 \times e_{100}$. The other two dotted lines show the expected distribution had the excesses been $2 \times e_{100}$ or $1 \times e_{100}$. The lower limit is calculated assuming that all the stars with $\chi_{100} < 3$ have no excess (double-dot–dashed line). (b) Same as (a) for wavelength 160 μm.
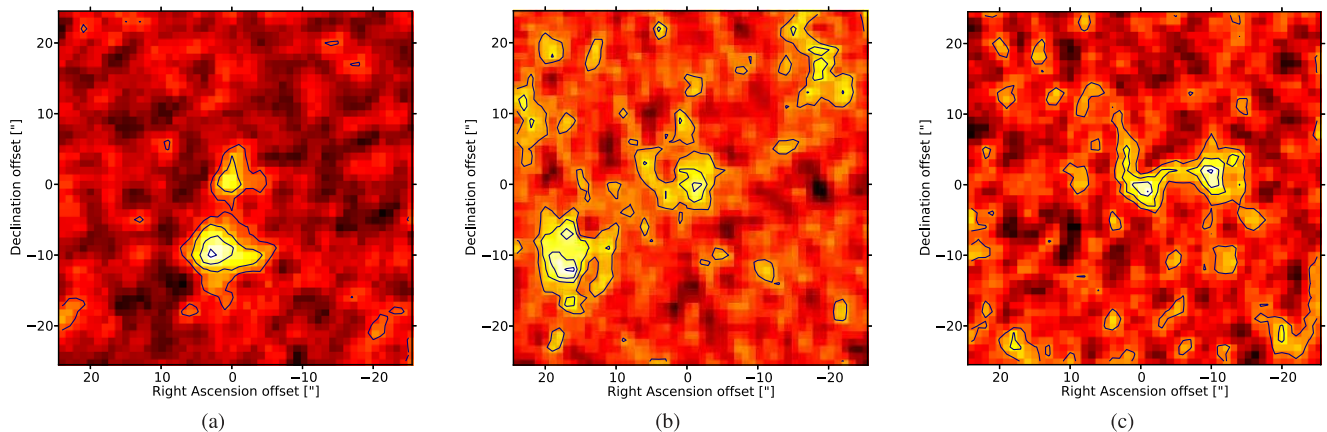
Figure 5. 100 μm maps centred on 25 Dra (a), s Eri (b) and 14 PsA (c). Colour scale is linear with contours indicating the 25, 50, 75 and 95 per cent of maximum flux levels

Table 3. Aperture photometry performed with GAIA on a selection of DEBRIS targets. Resolved debris discs around A stars in the *Herschel* DEBRIS survey and closest background object.

ID	F_{100}^{aper} (mJy)	$F_{100}^{\mathrm{bckgrd}}$ (mJy)	P_{100} (mJy)	Separation (arcsec)
25 Dra	9.26	19.70	8.36 ± 0.13	10.0
s Eri	6.88	13.27	6.59 ± 0.11	20.6
14 PsA	7.63	5.76	7.19 ± 0.14	11.0

shows the excess detection threshold at 100 μm while the dot–dashed line shows the excess detection threshold at 160 μm. The combination of the ages of the debris disc candidates and the higher threshold hinders the detection of discs with smaller radii (i.e. higher temperatures).

When the debris discs are resolved it is possible to measure the angular size of the disc from the images, see Booth et al. (2013) for a detailed study of the resolved debris discs around A stars in the

Herschel DEBRIS survey. They derived resolved radii for nine of the DEBRIS A stars (marked with an asterisk in Table 2) and found that the resolved radii vary from $\sim 1 \times$ to $\sim 2.5 \times$ the blackbody radii.

3.3 Disc mass

The disc mass can be derived from the fractional luminosity and disc radius as described by equation 7 from Wyatt (2008):

$$M_{\mathrm{disc}} = 12.6 f_{\mathrm{d}} (R_{\mathrm{disc}}^{\mathrm{cold}})^2 \kappa_\nu^{-1} X^{-1}, \tag{1}$$

where M_{disc} is in $M_\oplus$, $R_{\mathrm{disc}}^{\mathrm{cold}}$ is in au, $\kappa_\nu = 45\,\mathrm{au}^2\,M_\oplus^{-1}$ and $X = (850/\lambda_0)^\beta$ is a factor that accounts for the modified emission spectrum for wavelengths greater than λ_0 as described in Section 2. Therefore, M_{disc} corresponds to the disc mass in millimetre-centimetre-sized dust that would be inferred from an 850 μm flux measurement using a standard opacity of $1.7\,\mathrm{cm}^2\,\mathrm{g}^{-1}$ for comparison with other submm studies. For a uniform approach, since resolved radii are not available for all the DEBRIS discs, blackbody radii are used to derive the dust masses. As a result, the estimated
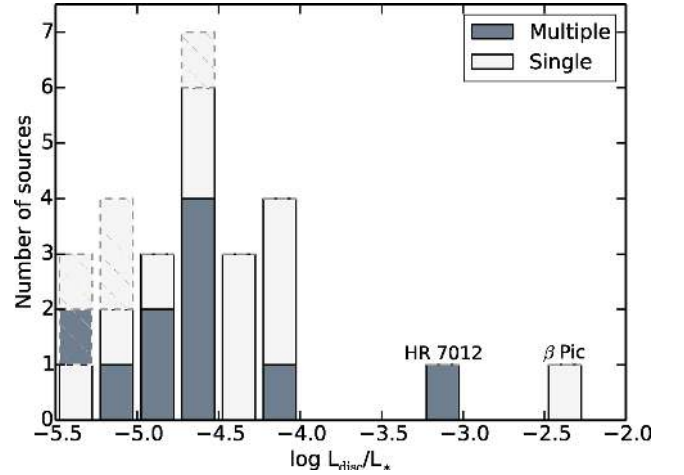
Table 4. Results from SED model fitting. The cold/hot designations for the two temperature disc models do not refer to specific temperature ranges but to one component being colder/hotter than the other one. The maximal fractional luminosities $f_{\max}$ are derived using the spectral types and ages listed in Table 2.

DEBRIS name	Name	ID	$T_{\mathrm{disc}}^{\mathrm{hot}}$ (K)	$R_{\mathrm{disc}}^{\mathrm{hot}}$ (au)	$T_{\mathrm{disc}}^{\mathrm{cold}}$ (K)	$R_{\mathrm{disc}}^{\mathrm{cold}}$ (au)	$f_{\mathrm{d}}^{\mathrm{cold}}$ $\times 10^{-5}$	M_{disc} $(M_\oplus)$	f_{d} $\times 10^{-5}$	$f_{\mathrm{d}}/f_{\max}$
Group I										
A003A	Vega	HD 172167	150 ± 28	23.9 ± 8.9	48 ± 6	235.1 ± 56.1	1.24 ± 1.17	8.9E−3 ± 1.0E−2	1.91 ± 1.30	0.03
A004A	Fomalhaut	HD 216956	145 ± 16	14.8 ± 3.3	37 ± 1	225.4 ± 17.6	5.09 ± 3.30	2.1E−2 ± 1.4E−2	6.33 ± 3.35	0.08
A005A	β Leo	HD 102647			114 ± 2	22.2 ± 0.9	2.18 ± 0.17	1.2E−4 ± 1.4E−5	2.18 ± 0.17	0.25
A014A	β Pic	HD 39060	487 ± 23	1.0 ± 0.1	107 ± 1	20.1 ± 0.6	208.55 ± 13.32	6.6E−2 ± 8.4E−3	323.10 ± 23.18	28.42
A016A	ζ Lep	HD 38678			173 ± 5	10.0 ± 0.7	8.90 ± 1.13	2.2E−4 ± 4.0E−5	8.90 ± 1.13	54.62
A018A	α CrB	HD 139006			126 ± 3	37.8 ± 1.7	1.73 ± 0.16	2.2E−4 ± 2.9E−5	1.73 ± 0.16	1.30
A021A	κ Phe	HD 2262			110 ± 8	22.0 ± 3.1	0.74 ± 0.22	9.3E−7 ± 3.8E−7	0.74 ± 0.22	1.00
A024A	β UMa	HD 95418			115 ± 5	44.8 ± 3.5	1.36 ± 0.27	4.1E−4 ± 1.1E−4	1.35 ± 0.27	0.49
A042A	21 Lmi	HD 87696			186 ± 21	7.2 ± 1.7	2.18 ± 0.88	2.2E−4 ± 1.4E−4	2.18 ± 0.88	23.00
A043A	HR 7012	HD 172555			289 ± 6	2.6 ± 0.2	71.24 ± 7.74	7.7E−4 ± 1.3E−4	71.24 ± 7.74	214.09
A053A	λ Boo	HD 125162	106 ± 6	28.5 ± 3.3	37 ± 5	236.4 ± 68.0	1.41 ± 1.20	4.4E−3 ± 5.6E−3	4.35 ± 1.59	0.03
A061A	ϵ Pav	HD 188228			84 ± 4	55.9 ± 5.4	0.44 ± 0.06	3.2E−5 ± 7.6E−6	0.44 ± 0.06	0.01
A064A	ζ Eri	HD 20320			77 ± 2	42.7 ± 2.4	1.90 ± 0.20	1.6E−4 ± 2.4E−5	1.90 ± 0.20	0.71
A067A	γ Tri	HD 14055	170 ± 35	14.2 ± 5.8	67 ± 2	90.7 ± 5.6	5.96 ± 0.37	2.4E−2 ± 6.6E−3	7.42 ± 1.46	0.18
A076A	ρ Vir	HD 110411	204 ± 71	6.8 ± 4.7	68 ± 13	60.0 ± 22.0	4.78 ± 5.60	4.1E−3 ± 6.2E−3	6.39 ± 6.25	1.07
A082A	30 Mon	HD 71155	451 ± 337	2.2 ± 3.3	108 ± 8	39.1 ± 6.0	2.89 ± 0.88	3.0E−4 ± 4.8E−4	4.85 ± 4.57	1.67
A086A	β Tri	HD 13161			87 ± 1	87.6 ± 2.6	3.10 ± 0.16	7.2E−3 ± 5.7E−4	3.10 ± 0.16	0.20
A103A	σ And	HD 1404			120 ± 14	26.5 ± 6.3	0.99 ± 0.59	1.3E−3 ± 9.8E−4	0.99 ± 0.59	1.01
A109AB	δ Scl	HD 223352	258 ± 166	6.0 ± 7.7	121 ± 34	26.8 ± 15.0	1.23 ± 0.40	3.0E−6 ± 1.2E−5	2.68 ± 4.68	0.70
A113A	HR 1139	HD 23281			147 ± 32	10.3 ± 4.5	3.89 ± 3.78	8.9E−5 ± 1.2E−4	3.89 ± 3.78	52.79
A123A	β PsA	HD 213398			120 ± 6	31.8 ± 3.2	1.20 ± 0.27	3.7E−6 ± 1.1E−6	1.20 ± 0.27	0.54
Group II										
A013A	ι Cen	HD 115892			156 ± 24	14.7 ± 4.5	0.73 ± 0.45	1.3E−7 ± 1.1E−7	0.73 ± 0.45	1.98
A051A	ι Ind	HD 198308			96 ± 45	28.0 ± 26.4	0.33 ± 0.38	9.4E−5 ± 2.1E−4	0.33 ± 0.35	0.66
A057A	q Vel	HD 88955			138 ± 21	19.3 ± 5.7	0.63 ± 0.36	3.6E−7 ± 3.0E−7	0.62 ± 0.39	0.12
A087A	60 Leo	HD 95608			153 ± 12	16.4 ± 2.5	2.57 ± 0.81	2.4E−6 ± 1.1E−6	2.18 ± 0.73	5.87
A120A	HR 7498	HD 186219			114 ± 47	19.5 ± 16.2	0.49 ± 1.45	6.8E−5 ± 2.3E−4	0.50 ± 1.18	0.97
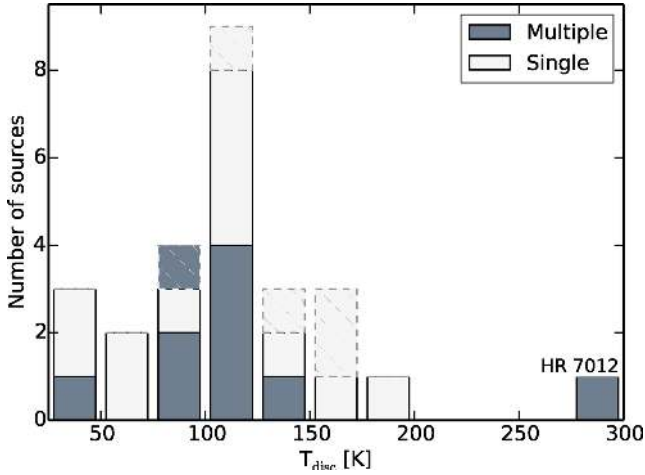
Figure 6. Dust temperatures for the debris discs in our A-star sample. Light shaded bars: the 12 single systems from group I. Dark shaded bars: the nine multiple systems from group I. Hatched bars: the five systems from group II.
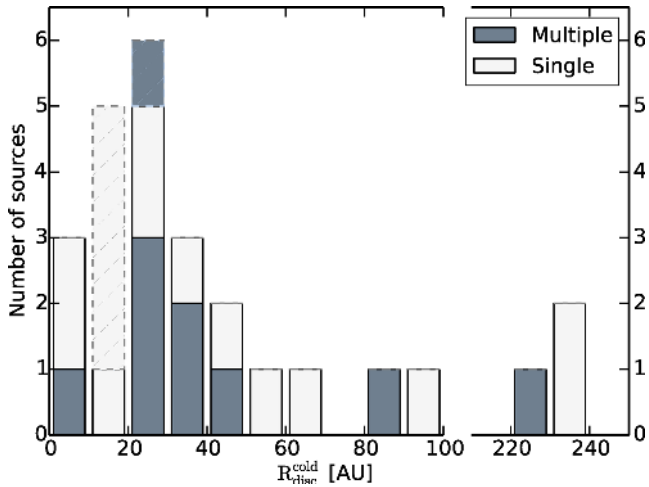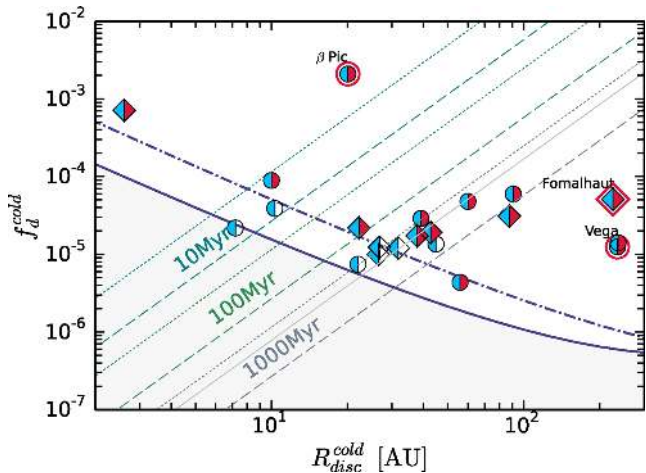

Figure 7. Fractional luminosity of the debris discs found around A-type stars. Light shaded bars: single systems from group I. Dark shaded bars: multiple systems from group I. Hatched bars: systems from group II.

dust masses are lower limits due to the resolved radii being 1–2.5× larger than the blackbody radii. The distribution of the dust masses found around our A-star sample is shown in Fig. 10. The masses we found range from $10^{-6.0}$ to $10^{-2.2}$ $M_\oplus$ with the median disc mass being $10^{-3.5}$ $M_\oplus$. These values can be compared to the estimated Edgeworth–Kuiper belt dust mass of $M_{\mathrm{KB}} = 10^{-5}$ $M_\oplus$ (Backman, Dasgupta & Stencel 1995).

In Fig. 11, we show a plot of M_{disc} as a function of $R_{\mathrm{disc}}^{\mathrm{cold}}$. We find that the median disc mass is lower for smaller discs (radii smaller than median blackbody radius), with $\tilde{M}_{\mathrm{disc}} \approx 10^{-3.8}$ $M_\oplus$, than for larger discs (radii larger than median blackbody radius), with $\tilde{M}_{\mathrm{disc}} \approx 10^{-2.4}$ $M_\oplus$. This is in agreement with the steady-state collisional model which predicts that the same initial mass closer to the star will be processed more quickly than material at greater distances. The dashed (dotted) lines show the expected $\propto 10^{13/3}$

Figure 8. Distribution of the blackbody disc radii derived from blackbody fits to our observations. Light-shaded bars: single systems from group I. Dark shaded bars: multiple systems from group I. Hatched bars: systems from group II.

Figure 10. Distribution of the disc mass derived from our estimated dust radial locations (R_{disc}^{cold}) based on inferred dust temperatures (T_{disc}^{cold}). Light shaded bars: single systems from group I. Dark shaded bars: multiple systems from group I. Hatched bars: systems from group II.
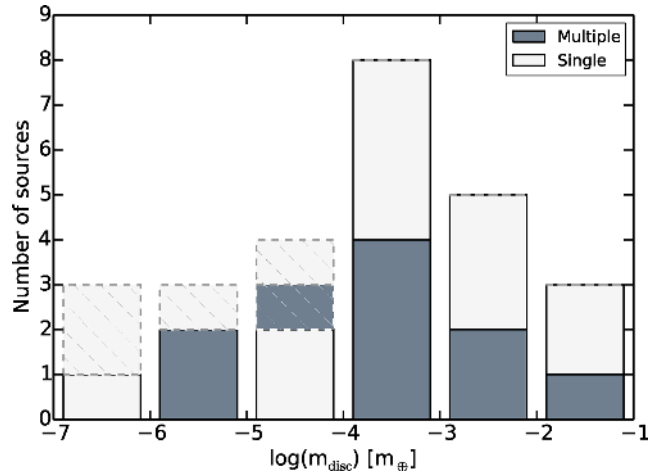

Figure 9. Fractional luminosity versus blackbody radius for A-stars debris discs. The circles are the single stars while the diamonds are the multiple systems. The left-filled symbols indicate stars with disc detection at 100 μm while right-filled symbols indicate stars with disc detection at 160 μm. The median detection thresholds at 100 and 160 μm are shown as solid and dash–dotted lines, respectively. The lines of maximum fractional luminosity, f_{max}, for ages of 10, 100 and 1000 Myr are shown with dashed lines for spectral type A0 and with dotted lines for spectral type A9. The sources located above the thin continuous grey line (which divides the sample into two bins) have a median age of 223 Myr while the source located below the thin continuous grey line have a medium age of 450 Myr indicating that older stars tend to be further to the right-hand side of the plot.
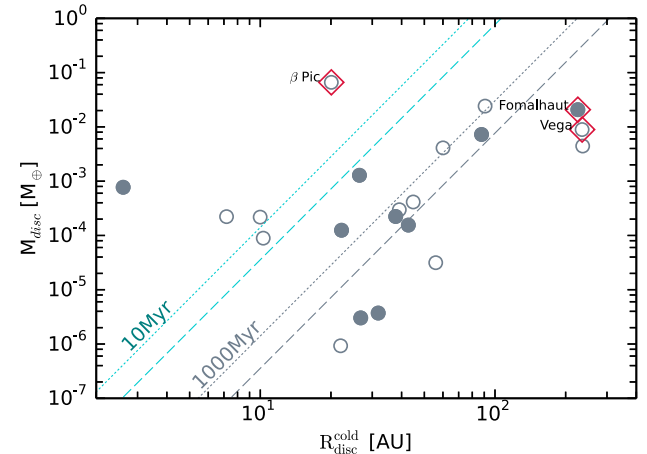
maximum mass inferred from the maximum fractional luminosity, f_{max} for the 10 and 1000 Myr old debris discs around A0 (A9) stars. The lines were calculated using $X = 22.83$, which is the median value for the DEBRIS sample.

3.4 Disc evolution

Although it is not possible to follow the evolution of individual discs, having a sample of debris disc systems spanning a large range of ages allows us to map the evolutionary trend of the disc population as a whole. Moreover, assuming all discs evolve


Figure 11. The circles represent the distribution of the disc mass as a function of the blackbody disc radius, with the shaded circles corresponding to multiple systems. Vega, Fomalhaut and β Pic are highlighted with red diamonds. The lines of maximum mass for ages of 10 and 1000 Myr are shown with dashed lines for spectral type A0 and with dotted lines for spectral type A9.

similarly, it can ultimately be used to refine disc evolution models. In order to generate plots of the excess ratios and fractional luminosities as a function of stellar age for all objects, we combined the DEBRIS data with age estimates taken from Vican (2012), Nielsen et al. (2013), Nakajima & Morino (2012), Zuckerman et al. (2011), Rebull et al. (2008), Monnier et al. (2012, Vega), Mamajek (2012, Fomalhaut) and Zuckerman et al. (2001, β Pic). For stars with two isochrone ages we used their averaged value as stellar age.

The evolution of 100 and 160 μm excesses with stellar age are illustrated in Figs 12(a) and (b). Both graphs show that there is a slow decay of the excesses as a function of stellar age (noted t hereafter) with a $\propto t^{-1}$ upper envelope. Moreover, our data show that the debris disc emission remains observable for the entire length of the main sequence with some substantial debris emission found around some of the oldest stars in our sample.

The distribution of the fractional luminosity as a function of stellar age is shown in Fig. 13. Also shown on this plot are evolutionary

(a)

(b)
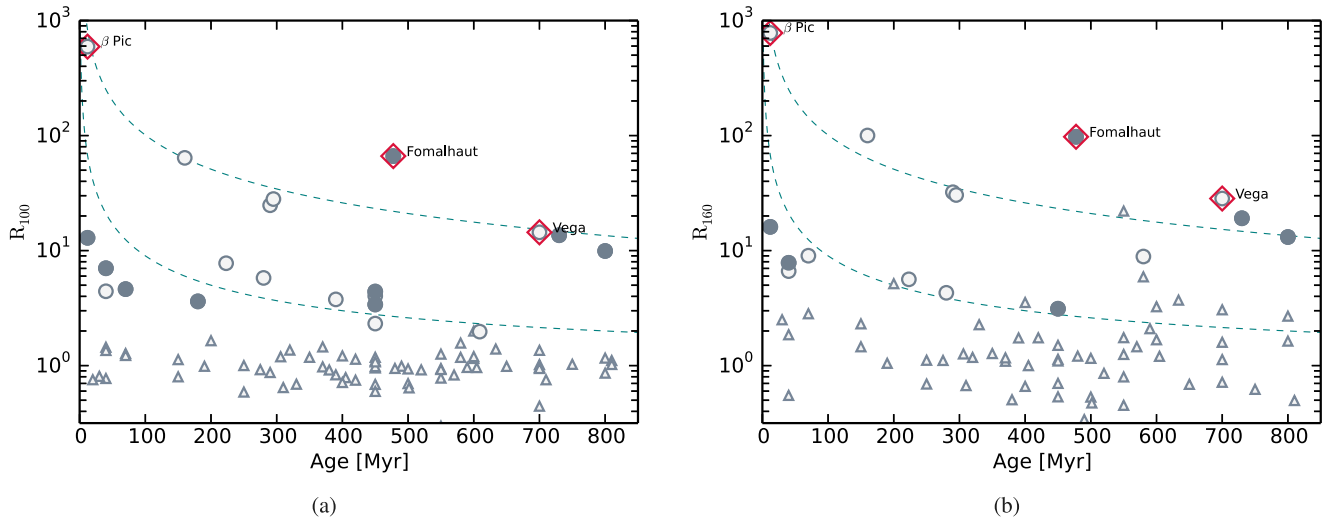
Figure 12. (a) 100 μm excess, R_{100}, versus age. Triangles: R_{100} for the systems where $\chi_{100} < 3$. Circles: R_{100} for the systems where $\chi_{100} \geq 3$, with the filled circles corresponding to multiple systems. Decay curves of $1 + t_0/t$ are plotted as dashed lines, with t in Myr and $t_0 = 10^4$, 800 Myr from top to bottom. t_0 is the characteristic time-scale of the fractional excess decay. (b) Same as (a) for wavelength 160 μm. Vega, Fomalhaut and β Pic are highlighted with red diamonds.
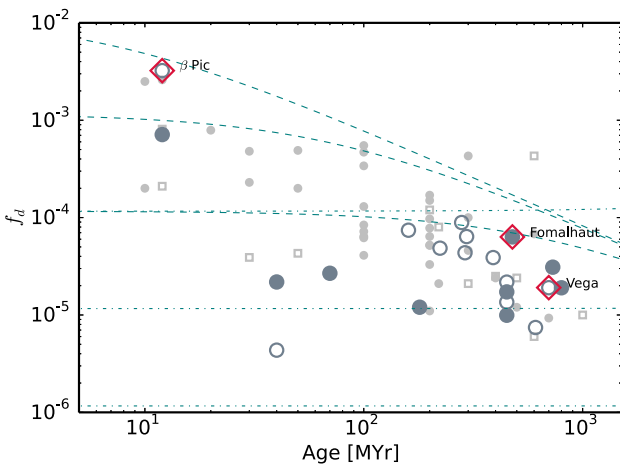
Figure 13. Fractional luminosity versus age of A-stars debris discs. The large open circles are single stars while the large filled circles are multiple stars. A-star data from Rodriguez & Zuckerman (2012), Fig. 7, are plotted with small circles being single stars and small squares multiple stars. Evolutionary tracks of planetesimal belts from Wyatt et al. (2007) are shown for disc radii of 10 (dashed lines) and 100 au (dashed–dotted lines) for initial disc masses of 1, 10 and 100 M$_\oplus$ from bottom to top. Vega, Fomalhaut and β Pic are highlighted with red diamonds.

tracks for planetesimal belts from Wyatt et al. (2007, fig. 5 left). The tracks are based on a steady-state collisional evolution model, which is one of the several models for debris disc evolution that have been proposed to interpret the data available to date. A detailed review of these models was presented by Wyatt (2008). They can be divided into two groups: steady-state collisional evolution models with or without delayed stirring, and stochastic models with infrequent collisions, dynamical instabilities or interactions with passing comets or stars. Steady-state collision models seem to hold true for most debris discs as was demonstrated by Wyatt et al. (2007). In such models, a collisional cascade is initiated resulting in planetesimals collisions which eventually grind them down to dust. The fractional luminosity remains constant until the largest planetesimals start to

collide and then follows a $\propto t^{-1}$ evolution, as illustrated in Fig. 13. The 100-au planetesimal belts (dash–dotted curves in Fig. 13) start with lower initial fractional luminosities and reach the turn over later than the smaller 10-au belts (dashed curves in Fig. 13). More massive discs start with higher fractional luminosities and reach the turn over earlier than less massive discs ultimately reaching the same values. Models that treat the collisional evolution of planetesimal belts in more detail find slightly different age dependences in different regimes (Löhne, Krivov & Rodmann 2008; Gáspár, Rieke & Balog 2013); however, these models can also be approximated reasonably well by a flat then 1/age fall-off.

The fractional luminosity data for the DEBRIS sample can be fitted with a $\propto t^{-0.65 \pm 0.09}$ power law as shown in Fig. 14, where the fractional luminosity is plotted as a function of stellar age with symbol sizes that scale up with the estimated blackbody radius of each disc. The slow fall-off rate originates from the DEBRIS sample being a collection of discs with a range of sizes and initial masses which each will follow their own evolutionary track. The larger discs population (blackbody radii larger than the median radius) have fractional luminosities that can be fitted with a $\propto t^{0.26 \pm 0.16}$ power law while for smaller discs the fractional luminosity follows a $\propto t^{-1.02 \pm 0.13}$ power law. This supports the prediction from the steady-state collisional evolution model described above.

4 DEBRIS DISC PARENT STARS

4.1 Properties of the parent stars

We have examined the occurrence of debris discs around A-type stars as a function of the properties of the parent stars with the 100 μm debris disc rate for each subsample being listed in Table 5. Our findings can readily be compared to the results from a similar study which was conducted by Phillips (2011) in the context of the MIPS-70 and MIPS-24 data.

We used their [M/H] metallicity data to establish the relationship between the disc detection rate and the metallicity [M/H]. The full A-star DEBRIS sample was split into two metallicity bins, [M/H] < 0 and [M/H] ≥ 0, with each bin consisting of 59 per cent
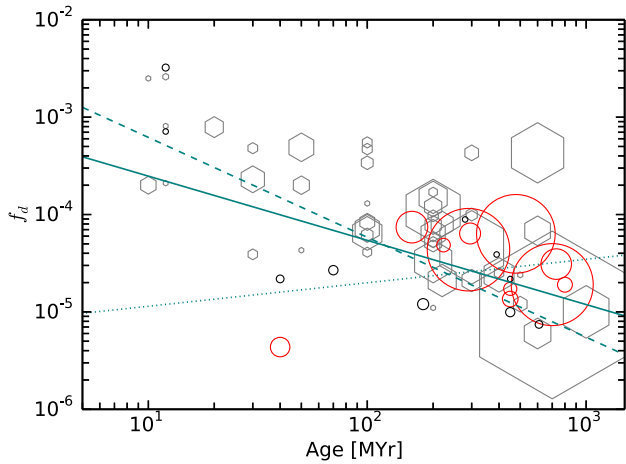
Figure 14. Circles: fractional luminosity versus age of A-stars debris discs. Grey hexagons: A-star data from Rodriguez & Zuckerman (2012) Fig. 7. Solid line: power-law fit to the group I, $f_d \propto t^{-0.65 \pm 0.09}$. Circles and hexagons sizes are scaled as a function of the blackbody disc radii. Dashed line: power-law fit to the group I systems with blackbody disc radii smaller than the median disc radius (black circles), $f_d \propto t^{-1.02 \pm 0.13}$. Dotted line: power-law fit to the group I systems with blackbody disc radii larger than the median disc radius (red circles), $f_d \propto t^{0.26 \pm 0.16}$.

Table 5. 100 μm occurrence of debris discs around A type as a function of the properties of the parent stars. Am and Ap stand for metallic and peculiar A stars, respectively.

Sample	N_{obs}	N_{disc}	Rate (per cent)
All	86	21	24 ± 5
$[M/H] < 0$	51	13	26 ± 6
$[M/H] \geq 0$	35	8	23 ± 7
$T_{eff} < 8200$ K	43	7	16 ± 6
$T_{eff} \geq 8200$ K	43	14	33 ± 7
$L_* < 19.8 \, L_{\odot}$	43	11	26 ± 7
$L_* \geq 19.8 \, L_{\odot}$	43	10	23 ± 6
$R_* < 2 \, R_{\odot}$	43	13	30 ± 7
$R_* \geq 2 \, R_{\odot}$	43	8	19 ± 6
Age$_* < 450$ Myr	43	14	33 ± 7
Age$_* \geq 450$ Myr	43	7	16 ± 6
Am	11	2	18 ± 12
Ap	5	1	20 ± 18
λ Boo	2	2	100

(51/86) and 41 per cent (35/86) of the whole sample, respectively. The debris disc detection rates in these two metallicity bins are similar with 26 ± 6 and 23 ± 7 per cent of the stars in each subsamples hosting debris discs. Thus, debris disc brightness does not depend on metallicity. Similar results had been found by Phillips (2011) for A-type stars and Greaves, Fischer & Wyatt (2006) for F/G/K-type stars.

In a similar manner, the A-star DEBRIS sample was split into two effective temperature bins at the median value of $\tilde{T}_{eff} \sim 8200$ K. The debris disc detection rates in these two temperature bins are 16 ± 6 and 33 ± 7 per cent, respectively. More discs are detected around the hotter stars in the DEBRIS sample which can be explained by the relationship between stellar effective temperature and age, with T_{eff} being higher for the younger stars. For stars older than 150 Myr, we find a −0.6 Pearson correlation coefficient between T_{eff} and the stellar age while for the younger stars there is no correlation.
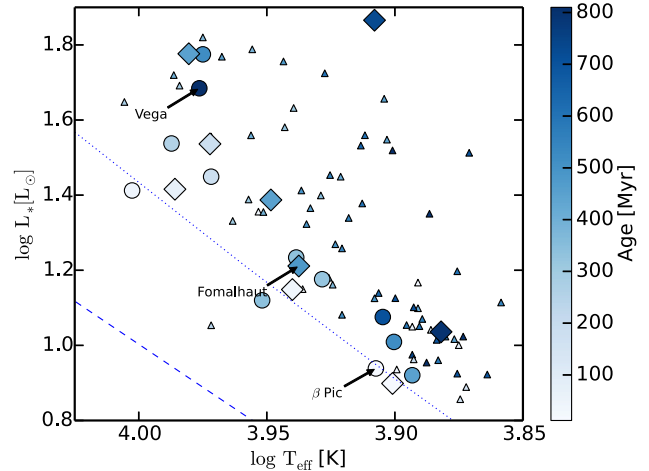
Figure 15. DEBRIS A stars placed in an H–R diagram with the debris systems being plotted with circles (single systems) and diamonds (multiple systems) and non-debris systems with triangles. The colour scale of the symbols is indicative of the age of the systems. The positions of the debris systems in this diagram show that the debris discs tend to be found around stars closer to the zero-age main sequence. Zero age main-sequence lines for $Z = 0.02$ and 0.001 (Schaller et al. 1992) are shown as dotted and dashed lines, respectively.

The disc incidence rate remains the same across the luminosity range with the number of detections being the same in the two luminosity bins split at the median value $\tilde{L}_* = 19.8 \, L_{\odot}$. Likewise, subsamples split at the median stellar radius $\tilde{R}_* = 2 \, R_{\odot}$ were studied, with a higher debris disc rate being found around the smaller A stars in our sample.

We finally looked at the debris disc occurrence into two age-split subsamples which was found to be higher amongst the younger stars in our sample as can equally be seen in Fig. 12(a). The age dependence of the debris disc detection is also demonstrated in Fig. 15 which places the DEBRIS A stars in an Hertzsprung–Russell (H–R) diagram with the debris systems being plotted with circles and non-debris systems with triangles, the colour of each symbol indicating the age of the system. The H–R diagram in Fig. 15 shows that younger stars, closer to the zero-age main sequence, are the most likely to have debris. Smaller stars (not yet swelling up above the main sequence) and hotter stars (shorter main-sequence lifetimes) thus tend to show debris more often. Higher luminosity stars are a blend of intrinsically young hot stars and more-evolved cooler stars, and so the debris incidence is an average over different ages, typical of the sample as a whole.

4.2 Multiplicity of the parent stars

With the typical orbital distances of companion stars and the extent of debris discs being similar, the properties of the debris discs can be expected to differ whether they belong to multiple systems or not. Companions dynamically influence the debris disc formation and evolution with, for example, the generation of gaps or truncated discs.

The DEBRIS A-star sample is comprised of 35 multiple systems and 51 single systems. The classification of multiplicity was made by Rodriguez et al. (in preparation) as part of a comprehensive multiplicity study of the DEBRIS stars. Debris discs have been detected in 9 of the multiple systems and 12 of the single systems therefore the disc detection rates are 9/35 (26 ± 7 per cent) and 12/51

Table 6. Disc properties for single versus multiple systems. The p-value indicates the likelihood of the two distributions being drawn from the same distribution. The higher the p-value, the higher the probability.

	Single	Multiple	Total	p-value
$\tilde{M}_{disc}(M_\oplus)$	3.6E−4	2.2E−4	3.0E−4	0.99
$\tilde{T}_{disc}$ (K)	107	120	110	0.99
$\tilde{f}_{disc}$	4.12E−5	2.18E−5	2.68E−5	0.99

(24 ± 6 per cent) for the multiple and single systems, respectively. Debris discs can be found around A stars irrespective of the presence of a companion, with similar incidence of debris discs among the single systems and the multiple systems. This contradicts the findings by Trilling et al. (2007) who found an incidence of debris discs higher in binary systems than around single stars. However, the difference has been subsequently attributed to the use of a lower disc detection threshold as extensively discussed by Phillips (2011).

We then used two-sample Kolmogorov–Smirnov tests (K–S test hereafter) in order to compare the distributions of the disc properties for single and multiple systems. We do not find any statistically significant dependance on multiplicity for the debris disc parameters (excess, temperature, fractional luminosity, radius and mass). Table 6 highlights some of the median disc parameters for both multiple and single systems. The median disc temperature for multiple systems is $\tilde{T}_{disc} = 120$ K which is comparable to the value found for single systems $\tilde{T}_{disc} = 107$ K. A K–S test performed on the two samples gives a p-value of 0.99 which signifies that they could have been drawn from the same distribution. The median fractional luminosity is almost twice as high for single systems, as was found by Rodriguez & Zuckerman (2012), with $\tilde{f}_d = 4.12 \times 10^{-5}$ compared to $\tilde{f}_d = 2.18 \times 10^{-5}$ for single and multiple systems, respectively. Nevertheless, a K–S test performed on the two distributions gives a p-value of 0.99 which indicates they could have being drawn from the same distribution.

Lastly we studied the occurrence of debris discs as a function of the companion separations. The multiple systems where debris discs are found fall into two categories: tight binaries with separations smaller than 1 au where the disc is circumbinary (separation/disc radius $<10^{-2}$) and wide binaries with separations greater than 100 au where discs are circumstellar (separation/disc radius >10). Within our sample, three discs are found to be circumbinary (α CrB, ζ Eri, β Tri) while six discs are found to be circumstellar (Fomalhaut, β Leo, HR 7012, σ And, δ Scl, β PsA). A histogram of the projected separations is shown in Fig. 16. The distribution is characterized by the absence of debris systems with intermediate separation (1–100 au), with the non-detection of debris discs within that separation range being a 1.7 per cent probability event under the hypothesis that debris discs systems have the same separation distribution as non-debris disc systems. Phillips (2011) found a similar gap with no systems having detected MIPS-24/MIPS-70 excess in the 3–150 au range. The lack of systems with 1–100 au separations was also observed by Rodriguez & Zuckerman (2012). In such systems, the disc/companion interaction leads to disc truncation and impacts its evolution by accelerating its dissipation. As such one can expect that the gap in the separation distribution does not originate from intermediate separation systems being less likely to host debris discs but from our sample comprising of systems (median age 450 Myr) which have already cleared out their discs. Based on our sample of debris systems, we conclude that discs around tight binaries and wide binaries are indistinguishable from discs around single stars.
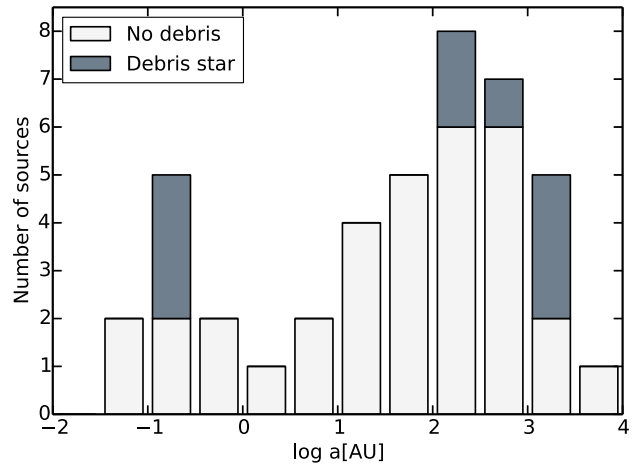
Figure 16. Stellar separation distribution. Open bars represent the systems without detected debris, while the shaded bars represent the debris stars. The median separation is 131 au.

The absence of debris systems with intermediate separation can be attributed to the system having evolved much faster due to the disc/companion interactions and the discs being undetectable.

5 SUMMARY

83 main-sequence A stars were observed at 100 and 160 μm as part of the DEBRIS project. Including the three Guaranteed Time Observations (GTO) targets forms an unbiased sample of 86 A stars. Within this sample, we detected debris disc excess emissions for 24 ± 5 per cent of our targets at 100 μm. Our debris disc detection rate is lower than what was previously found for A stars (Su et al. 2006; Phillips 2011) and is comparable to the debris disc rate around main-sequence F/G/K stars. However, this is a lower limit and we cannot exclude that the excess rate could be as high as 51 per cent at the median detection threshold of 1.70.

We find that the amount of detected excess emission decreases with stellar age as previously established by Rieke et al. (2005). However, debris discs with large excesses are found around some of the oldest stars in our sample, leading to the conclusion that the debris phenomenon can survive throughout the entire length of the main sequence which is consistent with the detection of debris disks around the subgiant descendants of main-sequence A stars (e.g. Bonsor et al. 2013).

Nevertheless, debris discs were detected predominantly around the youngest and hottest stars of our sample with 2/3 of the discs being found around stars younger that the median age (<450 Myr) of our sample.

No dependence of the debris disc incidence rate on the stellar metallicity nor on the stellar luminosity was found.

We found that the occurrences of debris discs around A stars in single and multiple systems are comparable. Similarly to Phillips (2011), we did not detect debris discs in systems with intermediate separations. The debris discs being found are either around tight <1 au or wide >100 au binaries. A likely explanation is that discs in intermediate systems have evolved much faster due to the disc/companion interactions and the discs have become undetectable to the limits of *Herschel*'s sensitivity. Finally, we found that the discs detected in tight and wide binary systems are statistically no different than discs around single stars.

REFERENCES

Acke B. et al., 2012, A&A, 540, A125
Aumann H. H., 1985, PASP, 97, 885
Aumann H. H. et al., 1984, ApJ, 278, L23
Backman D. E., Paresce F., 1993, in Levy E. H., Lunine J. I., eds, Protostars and Planets III. Univ. Arizona Press, Tucson, p. 1253
Backman D. E., Dasgupta A., Stencel R. E., 1995, ApJ, 450, L35
Bessel M. S., 1990, A&AS, 83, 357
Bonsor A., Kennedy G. M., Crepp J. R., Johnson J. A., Wyatt M. C., Sibthorpe B., Su K. Y. L., 2013, MNRAS, 431, 3025
Booth M. et al., 2013, MNRAS, 428, 1263
Chen C. H. et al., 2006, ApJS, 166, 351
Chen C. H. et al., 2007, ApJ, 666, 466
Chen C. H., Sheehan P., Watson D. M., Manoj P., Najita J. R., 2009, ApJ, 701, 1367
Chen C. H., Mittal T., Kuchner M., Forrest W. J., Lisse C. M., Manoj P., Sargent B. A., Watson D. M., 2014, ApJS, 211, 25
Chini R., Kruegel E., Kreysa E., Shustov B., Tutukov A., 1991, A&A, 252, 220
Churcher L. J. et al., 2011, MNRAS, 417, 1715
Cutri R. M. et al., 2003, 2MASS All Sky Catalog of Point Sources, available at: http://irsa.ipac.caltech.edu/applications/Gator/
Eiroa C. et al., 2013, A&A, 555, A11
Gáspár A., Rieke G. H., Balog Z., 2013, ApJ, 768, 25
Greaves J. S., Wyatt M. C., 2003, MNRAS, 345, 1212
Greaves J. S., Fischer D. A., Wyatt M. C., 2006, MNRAS, 366, 283
Habing H. J. et al., 2001, A&A, 365, 545
Hahn J. M., Malhotra R., 2005, AJ, 130, 2392
Hauck B., Mermilliod M., 1998, A&AS, 129, 431
Høg E. et al., 2000, A&A, 355, L27
Holland W. S. et al., 1998, Nature, 392, 788
Holland W. S. et al., 2003, ApJ, 582, 1141
Holmes E. K., Butner H. M., Fajardo-Acosta S. B., Rebull L. M., 2003, AJ, 125, 3334
Ishihara D. et al., 2010, A&A, 514, A1
Jewitt D. C., Luu J., 2004, Nature, 432, 731
Kennedy G. M., Wyatt M. C., Sibthorpe B., Phillips N. M., Matthews B. C., Greaves J. S., 2012, MNRAS, 426, 2115
Kenyon S. J., Bromley B. C., 2002, ApJ, 577, L35
King J. R., Villarreal A. R., Soderblom D. R., Gulliver A. F., Adelman S. J., 2003, AJ, 125, 1980
Liseau R., Brandeker A., Fridlund M., Olofsson G., Takeuchi T., Artymowicz P., 2003, A&A, 402, 183
Lisse C. M., Chen C. H., Wyatt M. C., Morlok A., Song I., Bryden G., Sheehan P., 2009, ApJ, 701, 2019
Löhne T., Krivov A. V., Rodmann J., 2008, ApJ, 673, 1123
Lykawka P. S., 2012, Monogr. Environ. Earth Planets, 1, 121
Lykawka P. S., Horner J., Jones B. W., Mukai T., 2009, MNRAS, 398, 1715
Mamajek E. E., 2012, ApJ, 754, L20
Matthews B. C. et al., 2010, A&A, 518, L135
Mermilliod J. C., 2006, VizieR Online Data Catalog, 2168, 0
Monnier J. D. et al., 2012, ApJ, 761, L3
Morales F. Y., Bryden G., Werner M. W., Stapelfeldt K. R., 2013, ApJ, 776, 111
Morbidelli A., Levison H. F., Tsiganis K., Gomes R., 2005, Nature, 435, 462
Morel M., Magnenat P., 1978, A&AS, 34, 477
Moshir M. et al., 1990, IRAS Faint Source Catalogue, version 2.0
Nakajima T., Morino J.-I., 2012, AJ, 143, 2
Nielsen E. L. et al., 2013, ApJ, 776, 4
Nilsson R., Liseau R., Brandeker A., Olofsson G., Risacher C., Fridlund M., Pilbratt G., 2009, A&A, 508, 1057
O'Brien D. P., Sykes M. V., 2011, Space Sci. Rev., 163, 41
Panić O. et al., 2013, MNRAS, 435, 1037
Phillips N. M., 2011, PhD thesis, Univ. Edinburgh
Phillips N. M., Greaves J. S., Dent W. R. F., Matthews B. C., Holland W. S., Wyatt M. C., Sibthorpe B., 2010, MNRAS, 403, 1089
Pilbratt G. L. et al., 2010, A&A, 518, L1
Plavchan P., Jura M., Lipscy S. J., 2005, ApJ, 631, 1161
Poglitsch A. et al., 2010, A&A, 518, L2
Rebull L. M. et al., 2008, ApJ, 681, 1484
Rieke G. H. et al., 2005, ApJ, 620, 1010
Riviere-Marichalar P. et al., 2014, A&A, 565, A68
Rodriguez D. R., Zuckerman B., 2012, ApJ, 745, 147
Schaller G., Schaerer D., Meynet G., Maeder A., 1992, A&AS, 96, 269
Sibthorpe B. et al., 2010, A&A, 518, L130
Su K. Y. L. et al., 2006, ApJ, 653, 675
Su K. Y. L. et al., 2013, ApJ, 763, 118
Trilling D. E. et al., 2007, ApJ, 658, 1289
Vandenbussche B. et al., 2010, A&A, 518, L133
Vican L., 2012, AJ, 143, 135
Vitense C., Krivov A. V., Kobayashi H., Löhne T., 2012, A&A, 540, A30
Williams J. P., Andrews S. M., 2006, ApJ, 653, 1480
Wilner D. J., Holman M. J., Kuchner M. J., Ho P. T. P., 2002, ApJ, 569, L115
Wright E. L. et al., 2010, AJ, 140, 1868
Wyatt M. C., 2008, ARA&A, 46, 339
Wyatt M. C., Smith R., Su K. Y. L., Rieke G. H., Greaves J. S., Beichman C. A., Bryden G., 2007, ApJ, 663, 365
Zuckerman B., Song I., Bessell M. S., Webb R. A., 2001, ApJ, 562, L87
Zuckerman B., Bessell M. S., Song I., Kim S., 2006, ApJ, 649, L115
Zuckerman B., Rhee J. H., Song I., Bessell M. S., 2011, ApJ, 732, 61

APPENDIX A: PACS PHOTOMETRY FOR NON DETECTION DEBRIS DISCS

Table A1. Observed and predicted PACS photometry. DEBRIS targets with no confirmed disc detections. Stellar ages are from Vican (2012). (*) The excess measured for 38 Ari (A077A, HD 17093) is due to a background galaxy, as shown by Panić et al. (2013).

DEBRIS name	Name	ID	Spectral type	Distance (parsec)	Age (Myr)	F100 (mJy)	P100 (mJy)	R100	χ_{100}	F160 (Jy)	P160 (Jy)	R160	χ_{160}
A002A	α Aql	HD 187642	A7Vn	5.12	700	329.02 ± 18.88	340.84 ± 8.07	0.97	−0.58	148.26 ± 9.94	131.54 ± 3.11	1.13	1.60
A006A	α Gem A	HD 60179	A1.5IV	14.00	250	34.55 ± 3.86	58.72 ± 0.29	0.59	−6.25	25.21 ± 9.47	22.67 ± 0.11	1.11	0.27
A007A	ι Uma	HD 76644	A7V(n)	14.51	750	35.49 ± 3.14	34.61 ± 0.76	1.03	0.27	8.30 ± 4.51	13.35 ± 0.29	0.62	−1.12
A011A	δ Leo	HD 97603	A4V	17.92	604.5	48.66 ± 3.95	50.65 ± 1.03	0.96	−0.49	23.50 ± 5.51	19.52 ± 0.40	1.20	0.72
A012A	β Ari	HD 11636	A5V	17.97	550	43.46 ± 3.35	46.15 ± 0.88	0.94	−0.78	14.17 ± 3.62	17.78 ± 0.34	0.80	−0.99
A015A	ε Ser	HD 141795	A2m	21.61	520	15.05 ± 2.31	16.40 ± 0.39	0.92	−0.58	5.41 ± 4.30	6.32 ± 0.15	0.86	−0.21
A017A	ζ Vir	HD 118098	A3V	22.72	490	23.32 ± 2.21	23.62 ± 0.47	0.99	−0.13	3.09 ± 4.30	9.10 ± 0.18	0.34	−1.40
A019A	δ Her	HD 156164	A3IV	23.04	350	33.55 ± 2.75	28.44 ± 0.54	1.18	1.82	13.96 ± 5.32	10.98 ± 0.21	1.27	0.56
A020A	9 Lib	HD 130841	A3IV	23.21	650	43.64 ± 3.38	44.33 ± 0.80	0.98	−0.20	11.74 ± 6.28	17.09 ± 0.31	0.69	−0.85
A022A	η Ind	HD 197157	A9IV	24.17	150	12.49 ± 2.19	11.09 ± 0.22	1.13	0.64	6.23 ± 4.68	4.27 ± 0.09	1.46	0.42
A023AB	γ Cet	HD 16970	A3V	24.35	500	15.05 ± 2.35	21.59 ± 0.42	0.70	−2.73	4.43 ± 3.66	8.33 ± 0.16	0.53	−1.06
A026A	δ UMa	HD 106591	A3V	24.69	450	24.34 ± 2.23	22.10 ± 0.44	1.10	0.99	9.65 ± 4.31	8.51 ± 0.17	1.13	0.27
A028AB	ζ UMa A	HD 116656	A2V	25.06	370	47.90 ± 3.60	49.19 ± 0.72	0.97	−0.35	20.74 ± 4.58	19.02 ± 0.28	1.09	0.38
A029A	γ Crt	HD 99211	A7V(n)	25.25	570	12.11 ± 2.48	14.62 ± 82.15	0.83	−0.03	8.22 ± 6.46	5.64 ± 31.70	1.46	0.08
A032A	γ UMa	HD 103287	A0Ve	25.51	450	41.99 ± 3.10	44.04 ± 0.66	0.95	−0.65	25.39 ± 5.11	16.95 ± 0.25	1.50	1.65
A034A	72 Oph	HD 165777	A4IVs	26.62	550	20.93 ± 2.61	16.65 ± 0.31	1.26	1.63	11.21 ± 5.64	6.41 ± 0.12	1.75	0.85
A035A	δ Crv	HD 108767	A0IV(n)	26.64	279.5	22.12 ± 2.28	24.03 ± 0.39	0.92	−0.83	10.24 ± 5.21	9.24 ± 0.15	1.11	0.19
A036AB	ζ Sgr	HD 176687	A2.5Va	27.03	480	41.28 ± 3.13	43.71 ± 0.90	0.94	−0.75	20.34 ± 5.01	16.84 ± 0.35	1.21	0.70
A038A	11 Eri	HD 18978	A3IV–V	27.17	633.5	19.25 ± 2.27	13.83 ± 0.31	1.39	2.37	19.80 ± 5.56	5.34 ± 0.12	3.71	2.60
A039A	59 Dra	HD 180777	A7V	27.30	450	5.01 ± 2.03	7.31 ± 0.12	0.69	−1.13	−1.18 ± 5.41	2.82 ± 0.04	−0.42	−0.74
A040A	β Eri	HD 33111	A3III	27.36	450	43.50 ± 3.37	44.37 ± 0.80	0.98	−0.25	18.77 ± 4.59	17.13 ± 0.31	1.10	0.36
A041A	θ Peg	HD 210418	A1Va	28.18	500	18.33 ± 2.00	19.61 ± 0.40	0.93	−0.63	8.75 ± 3.77	7.57 ± 0.15	1.16	0.31
A045A	f UMa	HD 78209	A1m	28.82	800	9.40 ± 1.84	10.94 ± 0.26	0.86	−0.83	11.34 ± 4.17	4.22 ± 0.10	2.69	1.63
A048A	ι Boo	HD 125161	A7V	29.07	40	6.22 ± 2.01	8.06 ± 0.18	0.77	−0.91	1.72 ± 4.35	3.12 ± 0.07	0.55	−0.32
A049A	α Pic	HD 50241	A7IV	29.40	700	36.02 ± 3.06	35.33 ± 0.67	1.02	0.22	9.77 ± 3.95	13.64 ± 0.26	0.72	−0.98
A056A	λ Gem	HD 56537	A3V	30.89	550	13.08 ± 2.13	16.81 ± 0.41	0.78	−1.71	2.92 ± 5.24	6.46 ± 0.16	0.45	−0.68
A063A	λ Psc	HD 222603	A7V	32.68	700	13.44 ± 1.99	9.91 ± 0.20	1.36	1.76	11.67 ± 3.47	3.82 ± 0.08	3.05	2.26
A065AB	β CrB	HD 137909	A9SrEuCrs	34.28	810	20.26 ± 2.54	18.32 ± 0.50	1.11	0.75	3.50 ± 3.42	7.04 ± 0.19	0.50	−1.03
A066A	67 UMa	HD 104513	A7m	34.28	150	4.71 ± 2.68	5.90 ± 0.10	0.80	−0.44	5.24 ± 4.46	2.27 ± 0.04	2.31	0.67
A068A	HR 4132	HD 91312	A7IV	34.63	420	6.39 ± 2.54	8.56 ± 0.19	0.75	−0.85	−3.14 ± 7.35	3.32 ± 0.07	−0.95	−0.88
A069A	α CVn A	HD 112413	A0spe...	35.25	190	20.03 ± 2.51	20.32 ± 0.37	0.99	−0.11	8.19 ± 3.65	7.82 ± 0.14	1.05	0.10
A071A	HR 4794	HD 109536	A7V	35.54	810	6.07 ± 2.16	5.94 ± 0.14	1.02	0.06	0.24 ± 3.43	2.29 ± 0.05	0.10	−0.60
A074A	18 UMa	HD 79439	A5V	35.84	710	5.97 ± 1.96	7.93 ± 0.13	0.75	−1.00	0.32 ± 4.00	3.07 ± 0.05	0.11	−0.69
A077A	38 Ari	HD 17093	A7III–IV	36.37	580	6.93 ± 1.95	5.89 ± 0.19	1.18	0.54	20.18 ± 5.10	2.27 ± 0.07	8.88	3.51
A078A	ι Cyg	HD 184006	A5V	37.22	450	22.64 ± 2.65	19.19 ± 0.39	1.18	1.29	3.97 ± 4.77	7.43 ± 0.15	0.53	−0.72
A079A	ξ Vir	HD 102124	A4V	37.41	501.5	4.48 ± 1.97	7.00 ± 0.18	0.64	−1.27	1.28 ± 3.36	2.71 ± 0.07	0.47	−0.43
A080A	16 Lyr	HD 177196	A7V	37.43	590	6.11 ± 1.93	6.34 ± 0.10	0.96	−0.12	5.13 ± 4.44	2.45 ± 0.04	2.09	0.60
A083AB	38 Lyn	HIP 45688	A3V	38.18	330	10.88 ± 2.46	15.81 ± 0.32	0.69	−1.98	13.83 ± 5.37	6.10 ± 0.12	2.27	1.44
A084A	α Vol	HD 78045	A5mA5V	38.28	420	14.61 ± 2.26	12.87 ± 0.24	1.14	0.76	8.64 ± 3.54	4.96 ± 0.09	1.74	1.04
A089A	ε Gru	HD 215789	A2IVnSB2	39.50	600	24.74 ± 2.51	21.45 ± 0.43	1.15	1.29	13.90 ± 3.44	8.29 ± 0.17	1.68	1.63
A090A	μ And	HD 5448	A5V	39.60	600	18.97 ± 2.11	15.85 ± 0.30	1.20	1.47	−3.30 ± 3.27	6.11 ± 0.11	−0.54	−2.88
A091A	10 Ser	HD 137898	A8IV	39.72	70	−0.27 ± 2.11	5.82 ± 0.10	−0.05	−2.88	−9.74 ± 6.08	2.25 ± 0.04	−4.34	−1.97
A092A	π Pav	HD 165040	A7sp	39.85	800	13.42 ± 2.49	11.56 ± 0.23	1.16	0.74	7.27 ± 4.11	4.46 ± 0.09	1.63	0.69
A093AB	γ Cen	HIP 61932	A1IV+	39.87	450	61.12 ± 3.85	56.75 ± 1.07	1.08	1.09	15.30 ± 5.30	21.86 ± 0.41	0.70	−1.23
A095A	τ Cen	HD 109787	A2V	40.25	310	8.68 ± 2.27	13.48 ± 0.22	0.64	−2.11	3.49 ± 5.66	5.21 ± 0.09	0.67	−0.30
A096A	60 Her	HD 154494	A4IV	40.90	400	6.79 ± 1.74	5.59 ± 0.11	1.21	0.68	7.62 ± 4.32	2.15 ± 0.04	3.54	1.26
A098A	g Leo	HD 85376	A5IV	40.96	450	3.15 ± 2.39	5.28 ± 0.11	0.60	−0.89	0.37 ± 3.38	2.04 ± 0.04	0.18	−0.49
A101A	109 Vir	HD 130109	A0V	41.24	290	11.62 ± 1.83	13.35 ± 0.29	0.87	−0.94	−1.74 ± 3.64	5.15 ± 0.11	−0.34	−1.89
A104A	HR 4086	HD 90132	A8V	41.48	70	6.67 ± 1.89	5.24 ± 0.09	1.27	0.75	18.24 ± 5.05	2.02 ± 0.03	9.03	3.21
A105A	10 Eri	HD 19107	A8V	41.56	70	6.24 ± 2.00	5.10 ± 0.11	1.22	0.57	5.57 ± 4.88	1.97 ± 0.04	2.82	0.74
A107AB	HR 5014	HIP 88726	A5V	41.79	20	5.09 ± 2.37	6.76 ± 0.12	0.75	−0.70	−2.02 ± 4.78	2.60 ± 0.04	−0.78	−0.97
A110A	λ UMa	HD 89021	A2IV	42.13	380	16.37 ± 1.95	17.88 ± 0.31	0.92	−0.77	3.47 ± 4.47	6.88 ± 0.12	0.50	−0.76
A118A	δ Hyi	HD 15008	A3V	42.81	405	8.06 ± 2.20	10.26 ± 0.18	0.79	−1.00	3.94 ± 3.99	3.95 ± 0.07	1.00	0.00
A119A	HR 8547	HD 212728	A4V	43.14	200	6.56 ± 1.90	3.99 ± 0.07	1.64	1.35	7.95 ± 4.25	1.54 ± 0.03	5.15	1.51
A121A	102 Aqr	HD 222345	A7IV	43.61	600	−0.28 ± 2.16	7.34 ± 0.17	−0.04	−3.52	−6.66 ± 4.52	2.84 ± 0.06	−2.35	−2.10
A127AB	γ CrB	HIP 76952	B9IV	44.62	400	8.31 ± 2.09	11.66 ± 0.34	0.71	−1.58	2.95 ± 4.54	4.48 ± 0.13	0.66	−0.34
A130A	η Hor	HD 16555	A6V	45.54	550	5.71 ± 2.27	6.17 ± 0.12	0.92	−0.21	2.98 ± 4.52	2.39 ± 0.05	1.25	0.13

APPENDIX B: PHOTOMETRY REFERENCES

Table B1. List of references for the photometry data used to perform SED model fitting for the DEBRIS targets.

Band	Wavelength (μm)	References
UBV	0.397, 0.491, 0.547	Mermilliod (2006)
HK	1.643, 2.275	Morel & Magnenat (1978)
RI	0.653, 0.803	Bessel (1990)
uvbyβ	0.507, 0.45, 0.450	Hauck & Mermilliod (1998)
BV (Tycho)	0.420, 0.532	Høg et al. (2000)
V (*Hipparcos*)	0.541	Hipparcos and Tycho Catalogues (ESA 1997)
*JK*s (2MASS)	1.238, 2.161	Cutri et al. (2003)
3.4, 12.22 (*WISE*)	3.353, 11.561, 22.088	Wright et al. (2010)
9, 18 (AKARI)	9, 18	Ishihara et al. (2010)
24, 70 (MIPS)	23.675, 71.420	Phillips (2011)
IRS (*Spitzer*)	6.504, 8.690, 11.435, 16.649, 22.942, 26.951, 30.957	Chen et al. (2006, 2007, 2009); Lisse et al. (2009) Su et al. (2013)
60, 170 (*ISO*)	60, 170	Habing et al. (2001)
12, 25, 60, 100 (*IRAS*)	12, 25, 60, 100	Moshir & et al. (1990)
70, 100, 160 (PACS)	70, 100, 160	Sibthorpe et al. (2010); Vandenbussche et al. (2010) Churcher et al. (2011); Kennedy et al. (2012) Acke et al. (2012); Booth et al. (2013)
250, 350, 500 (SPIRE)	250, 350, 500	Sibthorpe et al. (2010); Vandenbussche et al. (2010) Churcher et al. (2011); Kennedy et al. (2012) Acke et al. (2012); Booth et al. (2013)
450, 850 (SCUBA)	450, 850	Holland et al. (1998, 2003); Williams & Andrews (2006)
870 (SMTO, LABOCA)	870	Holmes et al. (2003); Nilsson et al. (2009)
1200 (SEST)	1200	Liseau et al. (2003)
1300 (MPIFR at SEST, IRAM PdBI)	1300	Chini et al. (1991); Wilner et al. (2002)
3300 (IRAM PdBI)	3300	Wilner et al. (2002)

APPENDIX C: ADDITIONAL A STARS

Table C1. Additional main-sequence A-type stars within our volume (distance <45 parsec) that were observed with *Herschel*/PACS.

Name	ID	Observation ID	Observing mode	Proposal ID	Notes	References
7 Ori	HD 31295	1342241872-73	PacsPhoto	OT1_hmaness_1	Excess detected with MIPS-70 *Spitzer* data *Herschel* data unpublished	Chen et al. (2014)
HR 1940	HD 37594	1342252043-46	PacsPhoto	OT2_nphillip_1	Excess detected with MIPS-70 *Spitzer* data *Herschel* data unpublished	Phillips (2011)
α CMa	HD 48915	1342183544-49	PacsPhoto	Calibration_pvpacs_29	*Herschel* data unpublished	
α Cir	HD 128898	1342205980-81	PacsPhoto	KPOT_ceiroa_1	No excess found heavy cirrus contamination	Eiroa et al. (2013)
d Sco	HD 146624	1342215617-20	PacsPhoto	KPOT_bdent_1	No excess found flux in agreement with photospheric emission	Riviere-Marichalar et al. (2014)
π Ara	HD 159492	1342243792-93	PacsPhoto	OT2_fmorales_3	Excess detected resolved debris disc	Morales et al. (2013)
γ Oph	HD 161868	1342231117-20	PacsPhoto	OT1_pabraham_2	Excess detected confirmed debris disc	Panić et al. (2013)

SUPPORTING INFORMATION

Additional Supporting Information may be found in the online version of this article:

Figure 1. SEDs for the Group I DEBRIS targets. (http://mnras.oxfordjournals.org/lookup/suppl/doi:10.1093/mnras/stu1864/-/DC1).

Please note: Oxford University Pres is not responsible for the content or functionality of any supporting materials supplied by the authors. Any queries (other than missing material) should be directed to the corresponding author for the paper.

This paper has been typeset from a TEX/LATEX file prepared by the author.